JGR Solid Earth

RESEARCH ARTICLE
10.1029/2020JB019863

On-Fault Geological Fingerprint of Earthquake Rupture Direction

J. Kearse[1,2] and Y. Kaneko[1,3]

[1]GNS Science, Lower Hutt, New Zealand, [2]School of Geography, Environment and Earth Sciences, Victoria University of Wellington, Wellington, New Zealand, [3]Department of Geophysics, Graduate School of Science, Kyoto University, Kyoto, Japan

Key Points:
- We develop a theoretical framework that links dynamic changes in coseismic slip direction with earthquake rupture direction for all faulting types
- The patterns of slickenline curvature previously documented for global historical earthquakes are consistent with model predictions
- Rupture directions of ancient, surface-breaking earthquakes can be determined using slickenlines preserved on fault surfaces

Supporting Information:
- Supporting Information S1

Correspondence to:
J. Kearse,
jesse@kearse.co.nz

Citation:
Kearse, J., & Kaneko, Y. (2020). On-fault geological fingerprint of earthquake rupture direction. *Journal of Geophysical Research: Solid Earth*, *125*, e2020JB019863. https://doi.org/10.1029/2020JB019863

Received 26 MAR 2020
Accepted 20 AUG 2020
Accepted article online 24 AUG 2020

Abstract How earthquake ruptures evolve and propagate are major outstanding questions in seismology. Our current understanding is limited to modern events captured by seismic networks, making it impossible to observe rupture propagation that occurred during earthquakes in the distant past. Here we propose a new method to discern the rupture propagation directions of past large earthquakes based on geological features preserved on fault slip planes. These features—called slickenlines—are striations formed during seismic slip and record dynamic fault movement during past surface-breaking earthquakes. We develop a theoretical framework that links slickenline curvature with rupture mode and rupture propagation direction for all faulting types and test our model using a global catalogue of historical surface-rupturing earthquakes with seismologically constrained rupture directions. Our results reveal that historical observations are consistent with theoretical predictions, thus providing a robust way to uncover the rupture directions of large earthquakes that lack instrumental data.

Plain Language Summary How earthquake ruptures evolve and propagate are major outstanding questions in seismology. Currently, we are unable to observe the details of earthquakes that occurred in the distant past, which limits our understanding to events recorded by modern technology. Here we propose a new method to uncover the rupture propagation direction of past large earthquakes, using geological features preserved on faults scarps. These features—called slickenlines—are scratch marks that form when two sides of a fault move past one another during an earthquake. We develop a theoretical framework that links the geometry of slickenlines with rupture propagation direction for all types of faults and test our model using a global catalogue of surface-breaking earthquakes. Our results reveal a strong link between our model and the available data, providing a new way to uncover the rupture direction of large earthquakes that are not recorded by modern seismic instruments.

1. Introduction

Extracting information about earthquake rupture dynamics from geological records remains one of the grand challenges in earthquake science. Striations on fault surfaces (referred to as *slickenlines*) are commonly documented in the field after surface-breaking earthquakes (Avagyan et al., 2003; Kearse et al., 2019; Otsubo, Shigematsu, et al., 2013; Shimamoto, 1996; Slemmons, 1957; Spudich et al., 1998; Xu et al., 2013) and form when one side of a fault scratches against the other during earthquake displacement. As such, slickenlines record the history and direction of coseismic slip and represent an important geological archive of dynamic faulting during past earthquakes.

However, inferring fault kinematics from the shapes of slickenlines is not straightforward because most documented slickenlines (~70%) from surface-rupturing earthquakes are either curved or misaligned with slip directions obtained using nearby offset features (Table 1). This kinematic mismatch appears to indicate that the direction of fault slip can change during the course of a single rupture (*rapid temporal changes in the direction of fault movement during seismic slip*) (Avagyan et al., 2003; Kearse et al., 2019; Otsubo, Shigematsu, et al., 2013; Shimamoto, 1996; Slemmons, 1957; Spudich et al., 1998; Xu et al., 2013). Although curved slickenline observations are widespread, the underlying cause for these changes is not yet clear. Previous interpretations of curved slickenlines have relied on complex and event-specific mechanisms, including the influence of a residual stress field due to a previous event nearby (Otsubo, Shigematsu, et al., 2013), cumulative slip of

Table 1
Historical Earthquakes for Which There are Documented Slickenline Observations

Earthquake	Mag	Mechanism	Max slip (m)	Slickenlines (SS) = supershear	Reference
1915 Pleasant Valley, United States	6.8	N	8.2	Linear	Jones (1915)
1937 Thuosou Lake, Tibet	7.5	SS-L	5.2	Linear	Guo et al. (2007)
1954 Fairview Peaks, United States	7.0	N SS-R	5.2	Curved	Slemmons (1957)
1957 Gobi-Altai, Mongolia	8.1	SS-L	7.0	Curved	Florensov and Solonenko (1965)
1959 Hegben Lake, United States	7.1	N	5.4	Linear	Witkind (1962)
1969 Pariahuancha, Peru	6.2	R	1.8	Curved	Philip and Megard (1977)
1974 Izu-Hanto-Oki, Japan	6.9	SS-R	1.0	Curved	Kakimi and Kinugasa (1977)
1980 El Asnam, Algeria	7.1	R	6.5	Curved	Philip and Meghraoui (1983)
1983 Borah Peak, United States	7.0	N	4.0	Linear	Crone et al. (1987)
1988 Tennant Creek, Australia	6.7	R	2.5	Unspecified	Crone et al. (1992)
1988 Spitak, Armenia	7.0	R	2.2	Curved	Avagyan et al. (2003)
1992 Landers, United States	7.3	SS-R	6.7	Curved	Arrowsmith and Rhoades (1994)
1995 Neftegorsk, Russia	7.6	SS-R	8.1	Curved	Shimamoto (1996)
1995 Kobe, Japan	7.2	SS-R R	2.5	Curved	Otsuki et al. (1997)
1999 Hector Mine, United States	7.1	SS-R	5.2	Linear	Treiman et al. (2002)
1999 Chi-Chi, Taiwan	7.6	R SS-R	16.4	Linear	Lee et al. (2003)
2001 Kunlun, Tibet	7.8	SS-L	16.3	Linear (SS)	Lin et al. (2002)
2002 Denali, Alaska	7.9	SS-R	8.8	Curved	Haeussler et al. (2004)
2008 Wenchuan, China	8.0	R SS-R	13	Curved	Pan et al. (2014)
2010 El Mayor-Cucapah, Mexico	7.2	SS-R	3.9	Curved	Fletcher et al. (2014)
2011 Fukushima, Japan	6.6	N	2.0	Curved	Otsubo, Shigematsu, et al. (2013)
2016 Kaikoura, New Zealand	7.8	SS-R	11.9	Curved	Kearse et al. (2018)

Note. N, normal; SS-L, strike-slip left lateral (sinistral); SS-R, strike-slip right lateral (dextral); R, reverse. Combinations of these refer to strongly oblique earthquake mechanisms. Modified from Kearse et al. (2019).

two discrete rupture episodes with different slip directions (Avagyan et al., 2003), and complex stress interactions near the junctions of intersecting faults (Xu et al., 2013).

A different view of curved slickenlines (Spudich et al., 1998) based on the theory of earthquake mechanics suggests that temporal changes in slip direction may instead be driven by dynamic stress changes on the sliding fault surface. This interpretation has led to the hypothesis that slickenline curvature could preserve the rupture propagation direction of past earthquakes (Figure 1a) (Kearse et al., 2019). Since rupture direction is an important parameter for our understanding of earthquake dynamics (Andrews & Ben-Zion, 1997; Harris & Day, 2005) and seismic hazard (Gerstenberger et al., 2020; Somerville et al., 1997), the ability to uncover the rupture direction of large historical earthquakes would help address related questions, including whether elastic contrasts across bi-material faults (Andrews & Ben-Zion, 1997) or locked-to-creeping transitions (Barbot et al., 2012) exert first-order controls on the direction of rupture propagation. However, a unifying theory linking curved slickenlines with rupture propagation direction remains undeveloped.

Here, we establish a theoretical link between rupture propagation direction and slickenline curvature using models of spontaneous dynamic rupture. We compare our findings with a catalogue of curved slickenlines from large historical earthquakes ($M_w > 6.5$) whose rupture directions are known from independent seismological data, to test whether slickenline curvature is controlled by the location and rake of the source mechanism and therefore whether it may be used to infer the direction of rupture propagation during past earthquakes.

2. Model Setup

To study the relationship between curved slickenlines and rupture direction, we consider idealized end-member fault kinematics. We keep our dynamic rupture models as general as possible by simulating

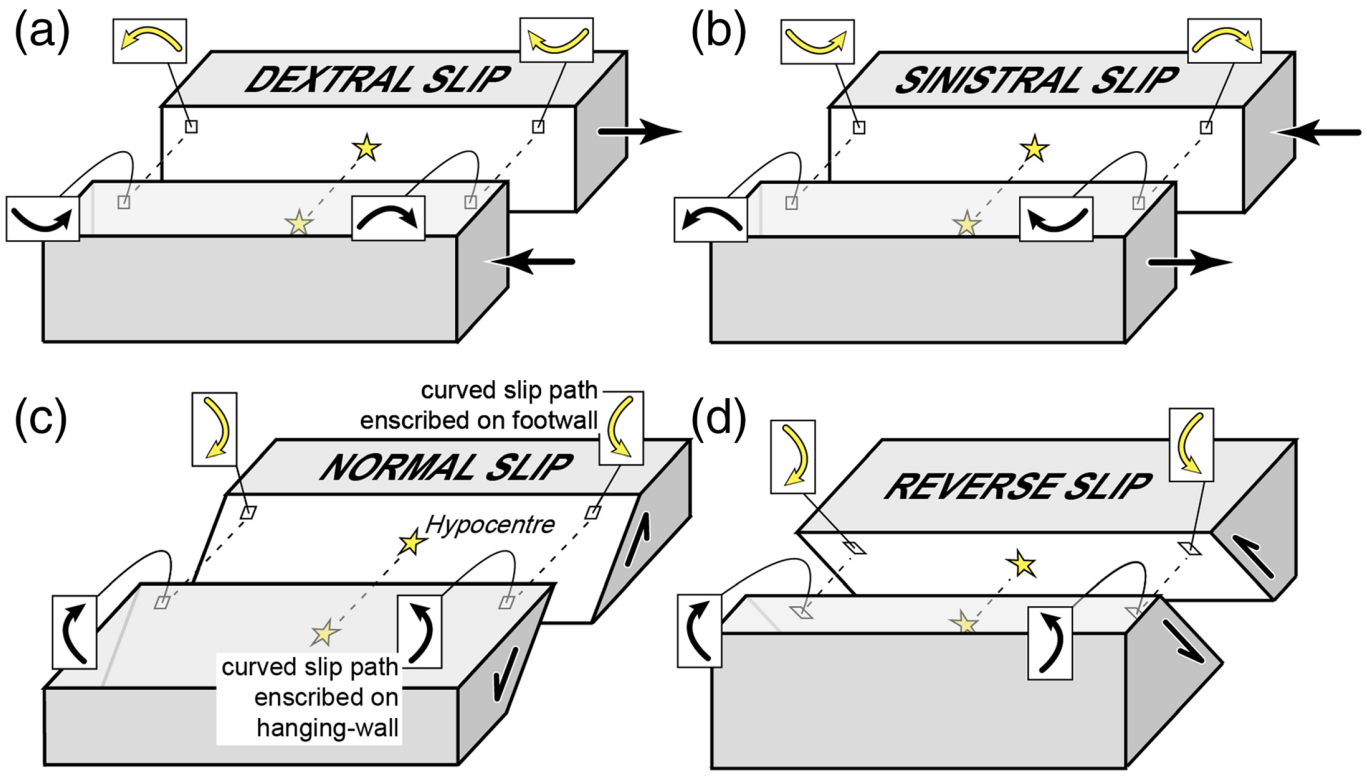

Figure 1. Curved slickenlines expected to form during surface-breaking earthquakes. For continuity, slickenlines are presented from the point of view of a geologist collecting data in the field. Yellow curved arrows represent motion of the near side of the fault relative to the far side; opposite is true for the black curved arrows. (a) Curved slickenlines expected to form on dextral strike-slip free faces. The sense of convexity (e.g., convex-up or convex-down) is related to the direction of rupture propagation, after Kearse et al. (2019). (b) Curved slickenlines expected to form on sinistral strike-slip free faces. (c) Curved slickenlines expected to form on normal fault free faces, with view toward the footwall. (d) Curved slickenlines expected to form on reverse fault free faces, with view toward the hanging wall. The sense of slickenline convexity (e.g., convex toward the hypocenter) is related to the direction of rupture propagation.

rupture on 2D Andersonian strike-slip (Figure 2a), normal (Figure 2b), and reverse faults (Figure 2c) each embedded within a 3D homogeneous elastic medium. Assigned wave speeds are 5.7 (*P* wave) and 3.3 km/s (*S* wave), and density is set to 2,700 kg/m^3. Normal stress and shear stress magnitudes are uniform along strike but increase linearly with depth (Figure 2 and Table S1). The constitutive response of each fault is governed by a linear slip-weakening friction law (Ida, 1972; Palmer & Rice, 1973), in which the shear strength of the fault linearly decreases from its static value τ_s to a dynamic value τ_d over a characteristic slip distance *Dc*. We assume that the slip velocity vector is parallel to the shear traction vector at each instant in time at all fault node points (Bizzarri & Cocco, 2003).

We assume that the time-independent effective normal stress $\sigma = \rho g z\,(1 - \lambda) = 7.4z$ (MPa), where g is gravity, z is down-dip distance in kilometer, and $\lambda = 0.73$ is the fluid pressure ratio (Harris et al., 2018). For simplicity, friction parameters (μs, μd, *Dc*) are assumed to be uniform over the fault plane. To suppress free surface-induced supershear ruptures that are not evident in real earthquakes, we further assume that frictional cohesion C is a piecewise linear function of depth and C = 2.0 MPa from the Earth surface down to 5-km depth and C = 0 MPa at greater depths. We vary friction and stress parameters in our models to test whether the sense of slip-path convexity depends upon these criteria.

The fault is initially at rest, and dynamic rupture is initiated by imposing a smooth, time-dependent growth of the rupture front within a 3-km nucleation patch located at 7.5-km down-dip distance at the center of the fault (solid black circles in Figure 2). The details of the nucleation procedure are described in benchmark problem TPV22 (Harris et al., 2018) (link: http://scecdata.usc.edu/cvws/). Once the rupture nucleates, it propagates spontaneously outside the nucleation patch. The numerical code we use is based on the spectral

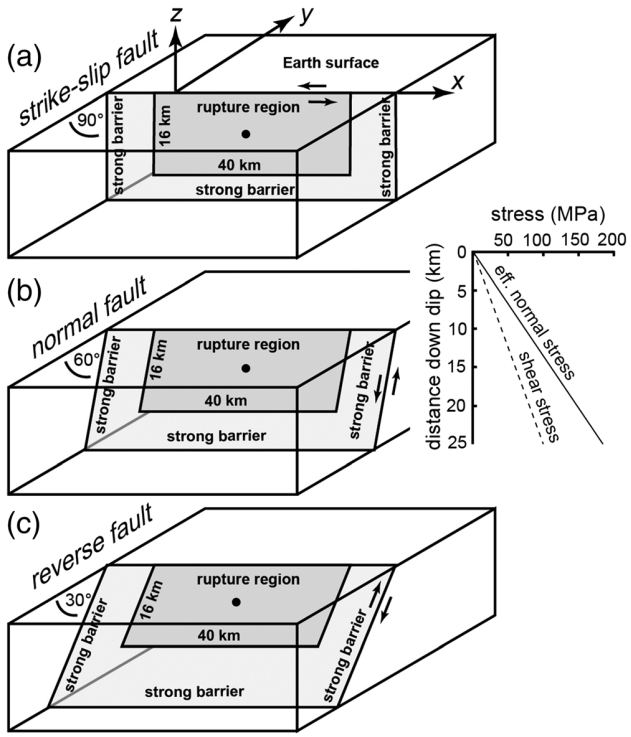

Figure 2. Andersonian fault models used in this study. (a) Sinistral strike-slip fault. (b) Normal fault. (c) Reverse fault. Solid black circles represent site of dynamic rupture nucleation. Dark gray area represents rupture region, and light gray area represents a strong barrier that arrests dynamic rupture. Inset shows the initial stress conditions on the fault surface.

element method (Ampuero, 2002; Kaneko et al., 2008), which has been verified through a series of community benchmark exercises (Harris et al., 2009, 2018).

3. Results

3.1. Dynamic Rupture Simulations

A series of snapshots of the three Andersonian dynamic rupture models are shown in Figures 3 (normal fault), 4 (reverse fault), and 5 (strike-slip fault). The left-hand panels within each figure illustrate the evolution of slip rate in m/s, while the right-hand panels show the evolution of instantaneous slip direction in degrees.

Our simulations demonstrate a systematic pattern of slip-path curvature that is linked to the direction of rupture propagation (Figure 6). We find that the mechanism proposed previously (Guatteri & Spudich, 1998; Spudich et al., 1998) is responsible for slip-path curvature: dynamic stresses generated within the process zone of a propagating rupture front produce temporal changes in slip direction. In this mechanism, dynamic stresses generated at the rupture tip induce transient stresses on the fault surface that are not aligned parallel to the initial shear traction direction and which are large enough to drive temporal changes in the direction of coseismic slip. Importantly, this only occurs along mixed-mode rupture directions (Andrews, 1994)—that is, along parts of the rupture tip where slip has components both perpendicular and parallel to the local rupture front (e.g., Figure 6a). Pure mode II (slip perpendicular to rupture front) or mode III (slip parallel to rupture front) rupture directions represent boundaries between adjacent mixed-mode domains (Figure 6). In particular, as a mixed-mode rupture approaches the Earth's surface (e.g., Figure 4), slip directions within the process zone begin to deflect away from prestress directions by $\leq$60°.

Although this process occurs across the entire width of the fault, it is enhanced near the free surface where confining stresses are always low relative to those at seismogenic depths (Figure 7a).

For dip-slip cases (Figures 6b and 6c), this transient change in rake angle introduces a component of strike-slip that is opposite in direction on either side of the hypocenter—dextral on one side (red colors) and sinistral on the other (blue colors). Dynamic strike-slip rupture (Figure 6a) produces transient components of vertical slip near the free surface that are either near-side up (blue colors to the right of hypocenter) or near-side down (red colors to the left of hypocenter). As further slip accrues, rake angles in all simulations rotate back toward the prestress direction, resulting in curved slip paths whose convexity points toward the hypocenter for both normal and reverse fault rupture and is either convex-up or convex-down for strike-slip rupture. Because distinct slickenline geometries are produced by specific rupture directions, they have the potential to preserve the direction of earthquake rupture propagation, independent of seismological data.

Earthquakes rarely involve pure dip-slip or pure strike-slip. As such, we also examine the effects of oblique prestress rake angles on the convexity of slip paths and on any along-strike variability in slip-path geometry (Figure 7b). To demonstrate the effects of obliquity, we change the rake angle of prestress in our normal fault model from −90° to −110°. In contrast to pure normal faulting (e.g., Figure 6b), the mode II boundary is not vertically aligned in oblique faulting simulations (Figure 7b). Due to the imposed clockwise rotation of the prestress rake angle, the mode II boundary between transient dextral-normal (red colors, Figure 7b) and sinistral-normal slip (blue colors, Figure 7b) at the free surface is shifted to the right of the hypocenter. As a result, this side of the fault ($x = 10$ km) experiences a reduced component of mixed-mode rupture as it is closer to the mode II boundary, producing only subtle slip-path convexity, whereas the left side of the fault ($x = -10$ km) receives rupture that is strongly mixed-mode (approximately equal components of slip perpendicular and parallel to the rupture rupture) and exhibits more pronounced slip-path convexity.

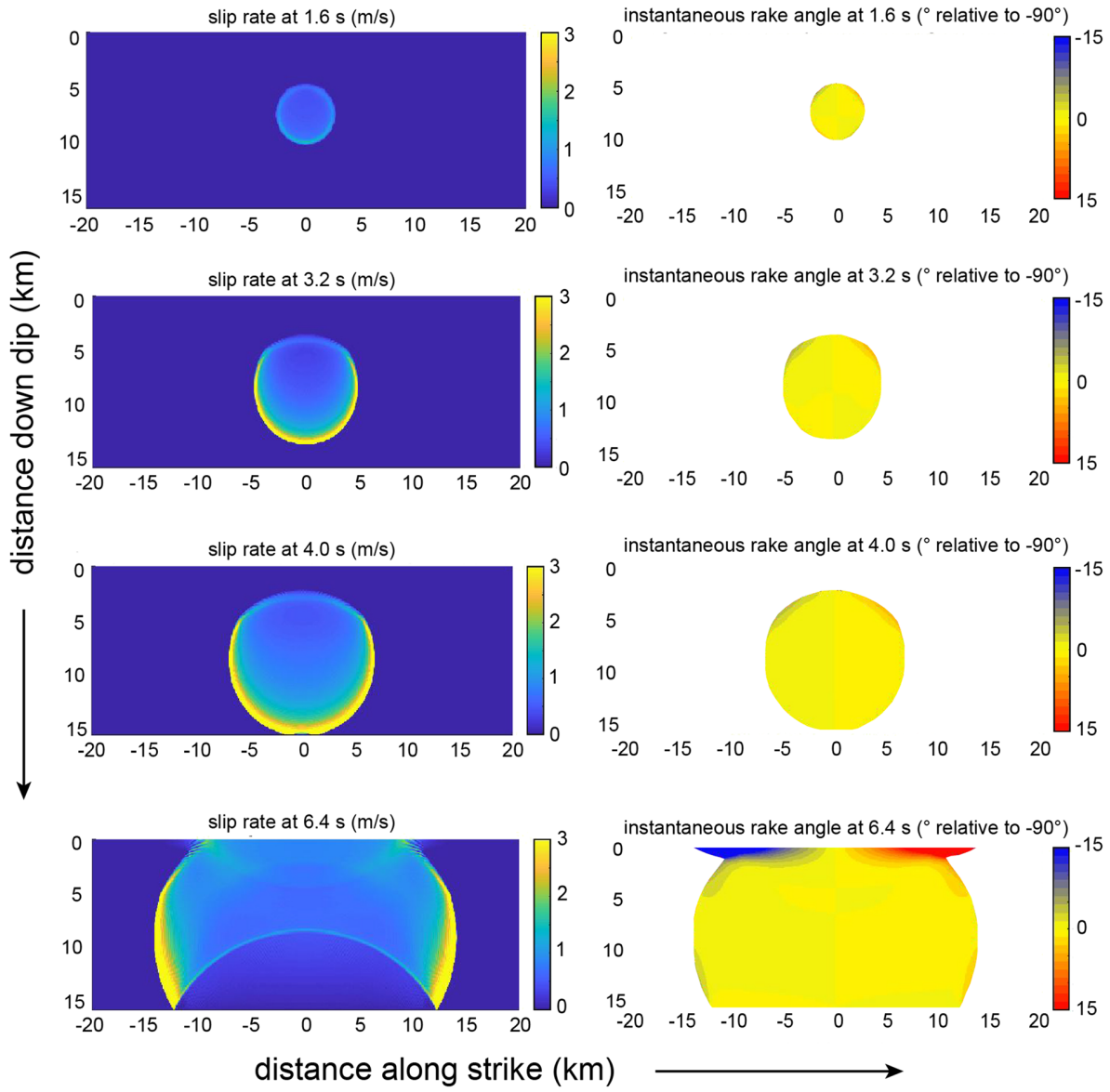

Figure 3. Snapshots of dynamic rupture for a 60° dipping normal fault. Left-hand panels show evolution of slip rate in m/s at selected time steps. Right-hand panel shows instantaneous slip direction for corresponding time steps.

To assess the reliability of our results, we prescribe within our simulations different friction parameters, initial stresses (weak vs. strong fault), and stress-drop magnitudes (Table S1). Although some parameter choices result in sharper slip-path convexity overall than others, the along-strike pattern (e.g., Figure 1) remains unchanged. Our results suggest that the underlying physical mechanism responsible for slip-path convexity during earthquake faulting is a robust feature that is independent of model assumptions, at least for plausible ranges of parameters.

3.2. Comparison With Historical Earthquakes

Here we test whether the theoretical relationship between dynamic rupture propagation and slip-path curvature applies to real earthquakes by compiling historical field observations of curved slickenlines, seismologically determined hypocentral locations, and focal mechanisms. Out of ~60 earthquakes with geologically documented surface rupture, we identify eight events for which all the necessary ingredients to test the

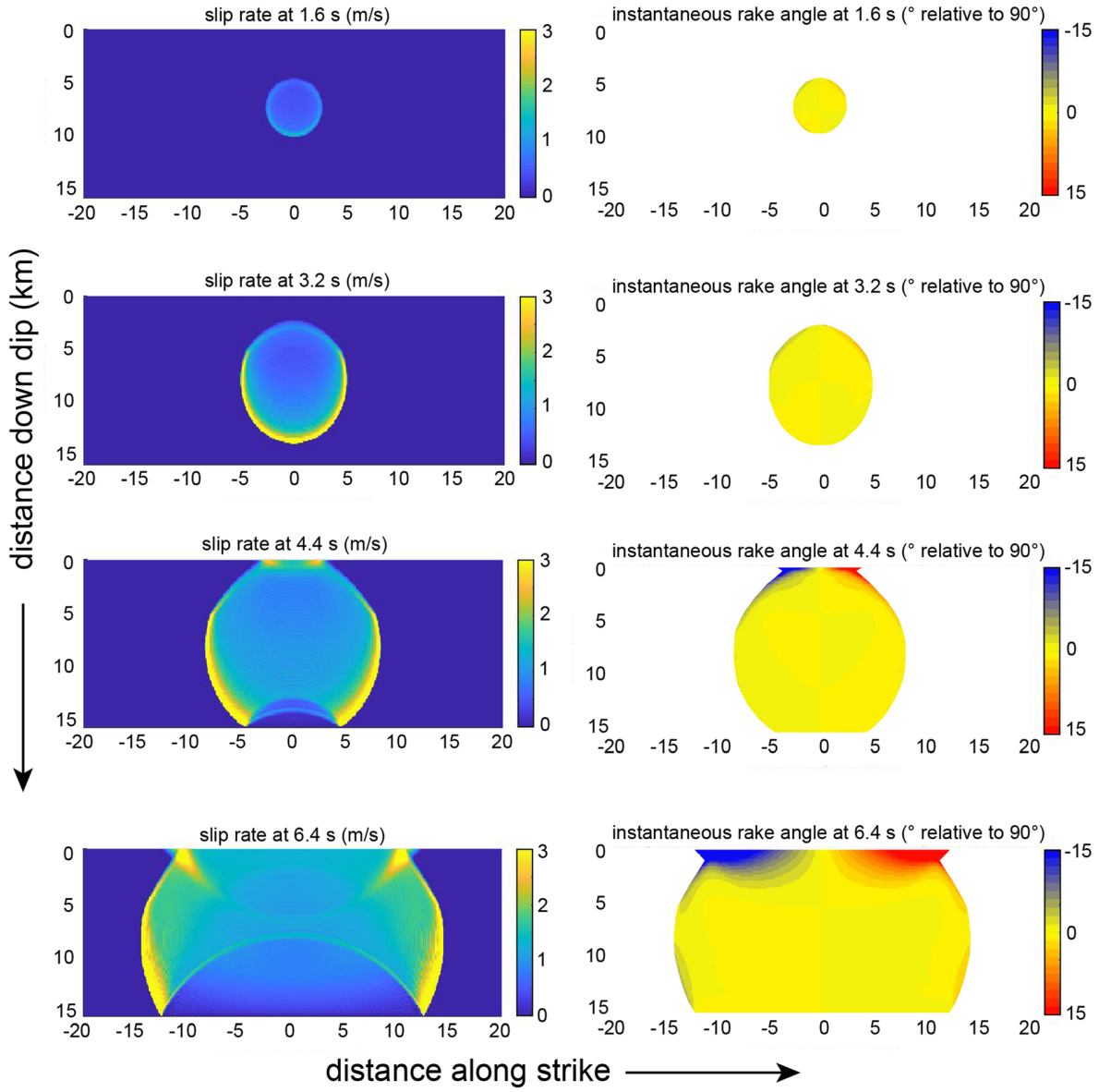

Figure 4. Snapshots of dynamic rupture for a 30° dipping reverse fault. Left-hand panels show evolution of slip rate in m/s at selected time steps. Right-hand panel shows instantaneous slip direction for corresponding time steps.

model are available (i.e., curved slickenlines, hypocenter location, and focal mechanism). These eight earthquakes, introduced below, occurred in different tectonic settings, with a variety of faulting types and magnitudes. Below, we summarize each event, including the relevant geological and geophysical data. We find that both slickenline convexity and rupture propagation direction in each of the eight earthquakes are matched by the results of our simple models.

3.2.1. 2011 M_w 6.6 Fukushima, Japan

The Fukushima earthquake produced 14 km of surface rupture on the southwest-dipping Itozawa normal fault and 16 km of surface rupture on the adjacent southwest-dipping Yunodake normal fault (Mizoguchi et al., 2012) (Figures 8 and 9a). Seismological studies (Tanaka et al., 2014; Toda & Tsutsumi, 2013) suggest that the earthquake nucleated near the southeast tip of the Itozawa fault at 5-km depth and propagated northwest along it. According to the analysis of Tanaka et al. (2014), as the rupture approached the

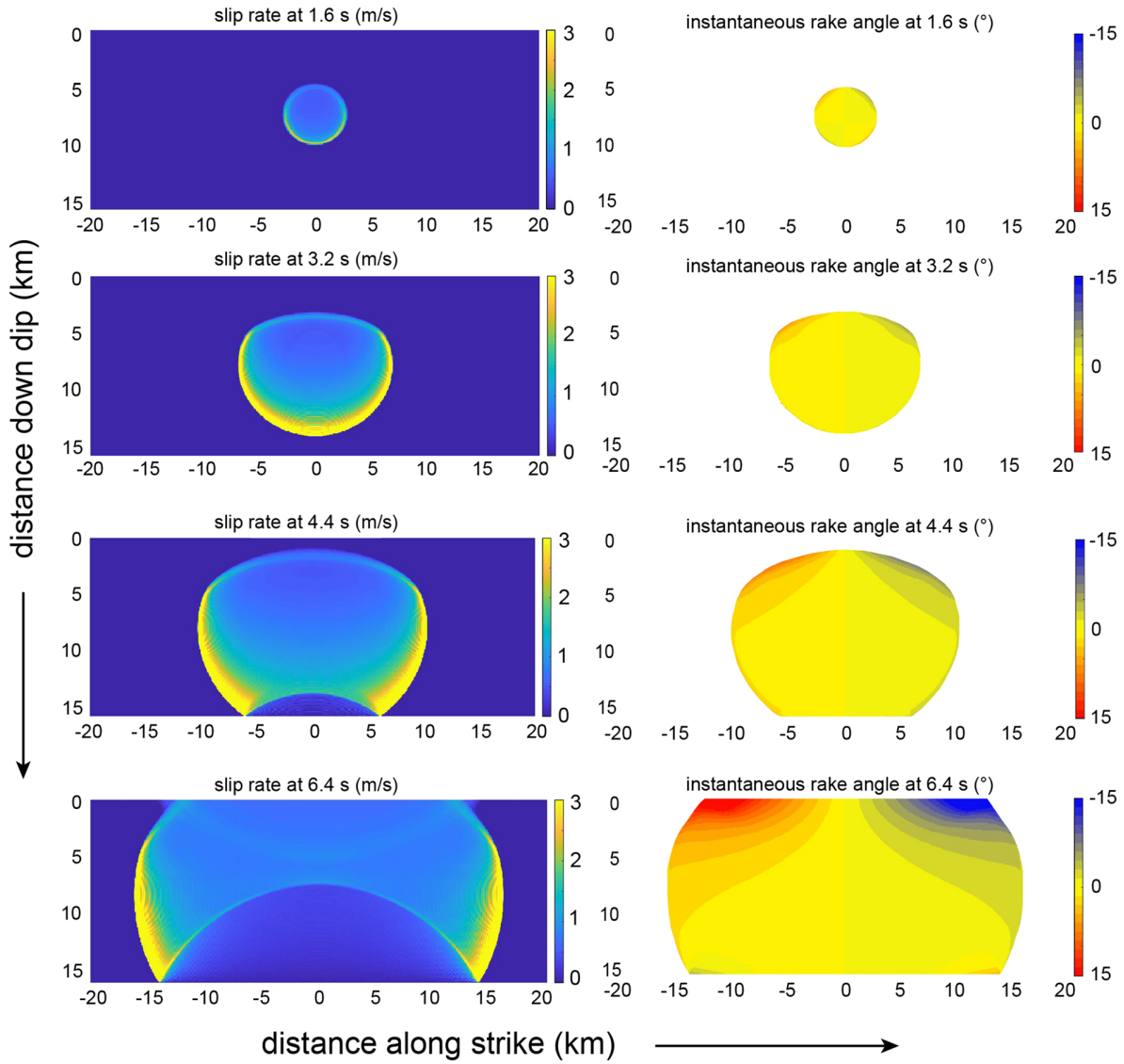

Figure 5. Snapshots of dynamic rupture for a 90° dipping sinitral fault. Left-hand panels show evolution of slip rate in m/s at selected time steps. Right-hand panel shows instantaneous slip direction for corresponding time steps.

northwest end of the Itozawa fault, it appears to have triggered a southeast-directed rupture on the sub-parallel Yunokade fault located <5 km to the east (Figure 8).

Vertical slip and scarp height at the surface trace of the Itozawa fault reached 2 m and exposed many striated free faces (Mizoguchi et al., 2012). Many slickenlines were documented—most of which were curved—and their convexity was consistent at all sites; curved slickenlines were convex toward the hypocenter (Figures 9a and 10a) (Otsubo, Shigematsu, et al., 2013). On the Yunodake fault, scarps were <1 m in height. Near the southeastern end of this fault rupture, linear slickenlines pitching toward the northwest at an angle of 60° were observed (Figure 8) (Mizoguchi et al., 2012), which describes dextral-normal slip on the southwest-dipping fault. These slickenlines can be traced to within a few centimeters of the top of the scarp, suggesting that they were formed early in the rupture. Yet the horizontal offset recorded by piercing points at this site was 20 cm in a sinistral sense. This implies that the direction of slip on the Yunodake fault changed during the earthquake; initial dextral-normal slip (recorded by slickenlines) was followed by a change to sinistral-normal slip (not recorded by slickenlines). The convexity implied by these observations on the

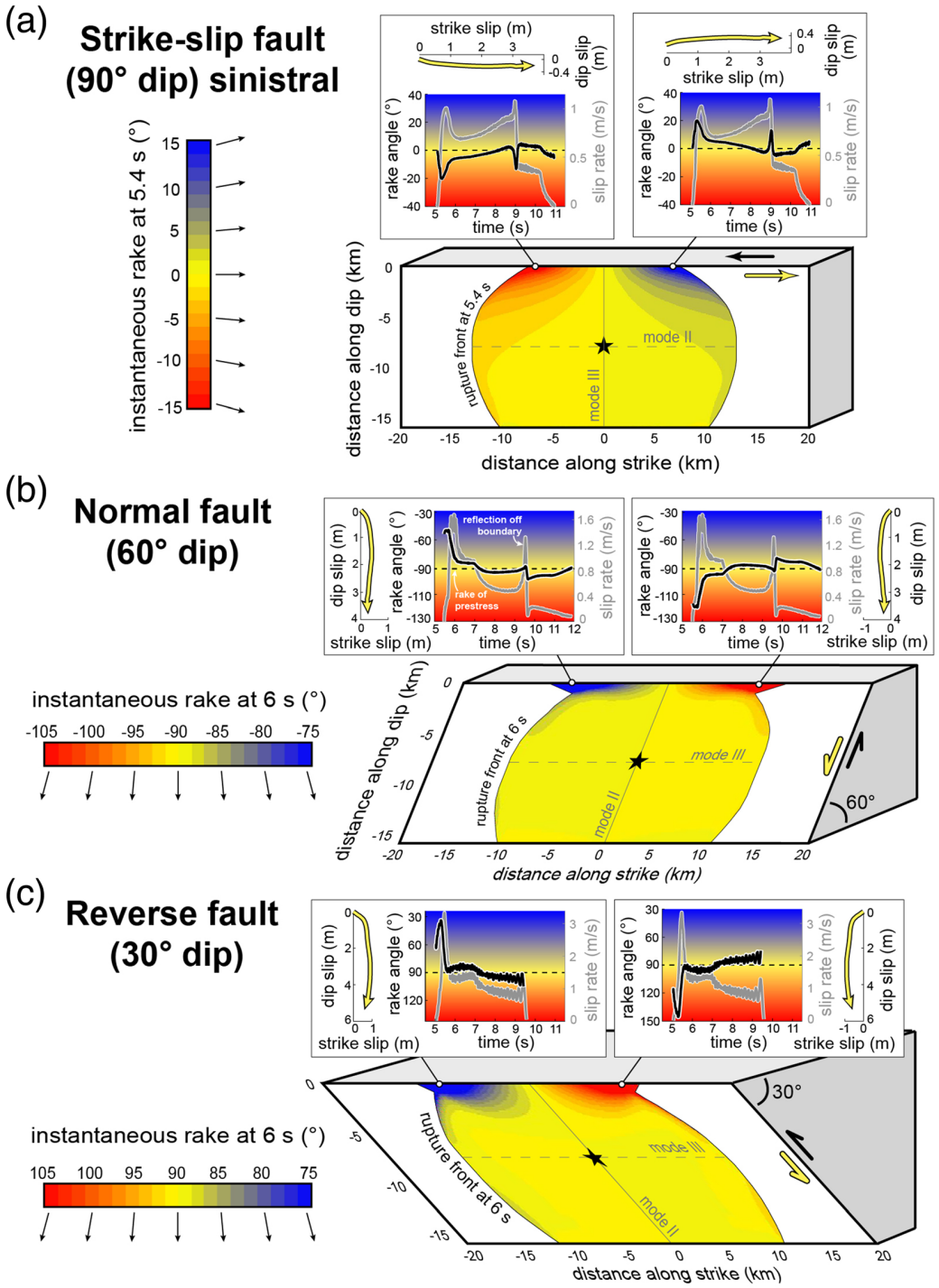

Figure 6. Fault plane view of dynamic rupture simulation results for tectonic faults. Colors describe the instantaneous slip direction of the near side of the fault relative to the far side, 5.4–6 s after rupture initiation. Panels located above fault planes show history of rake angle and slip rate at each end of the rupture (at x = −10 km, and x = 10 km), and the yellow arrows depict their corresponding slip paths (slickenlines). Mode II rupture shown as solid line through hypocenter and mode III rupture shown as dashed line through hypocenter. (a) Vertical strike-slip fault with a prestress rake angle of 0°. Note that subtle rake changes along mode II direction represent boundary artifacts. (b) Normal fault with 60° dip and a prestress rake angle of −90°. (c) Reverse fault with 30° dip and a prestress rake angle of 90°.

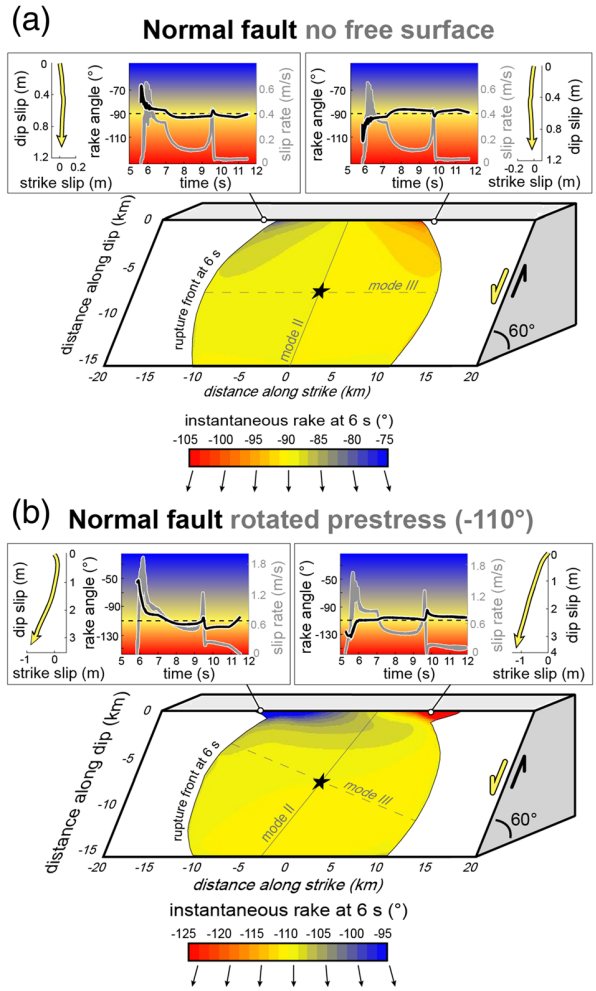

Figure 7. Simulations of dynamic rupture under different boundary conditions. (a) Normal fault with 60° dip and without a free surface. We simulate a lack of free surface by nucleating the rupture 20 km deeper, while maintaining the same stress and friction conditions as the equivalent simulation shown in Figure 6b. (b) Normal fault with 60° dip and an oblique prestress rake angle of −110°. The oblique prestress direction increases the mixed-mode component of rupture at the surface between x = −10 km and x = 0 km, while reducing it between x = 0 km and x = 10 km. This is reflected in the convexity of the resulting slip paths. Note that subtle rake changes along mode II direction represent boundary artifacts.

Yunodake fault is opposite in direction to the convexity of slickenlines seen on the Itozawa fault (Figure 8). According to our model results, this is consistent with the proposed opposite direction of rupture propagation on both faults (e.g., Figures 9 and 11a). For simplicity and continuity between the eight historical earthquakes shown in Figures 9 and 10, we show only the primary observations on the Itozawa fault.

3.2.2. 1995 M_w 7.2 Kobe, Japan

The Kobe earthquake of January 1995 ruptured a series of strike-slip faults near Osaka Bay, Japan, over a combined length of ~50 km (Yoshida et al., 1996). The rupture nucleated at 12-km depth at the junction of Nojima and Suma faults and ruptured bilaterally, extending ~20 km southwest along the Nojima fault where it produced surface slip of up to 2 m and ~30 km to the northeast on the Suma, Suwayama, and Gosukebashi faults underneath Kobe city where it did not rupture the ground surface (Yoshida et al., 1996) (Figure 9b).

At several sites southwest of the hypocenter on the Nojima fault, overhanging free faces were observed with curved slickenlines showing clear temporal changes in slip direction (Figures 9b and 10b) (Otsuki et al., 1997; Spudich et al., 1998). The slickenlines pitch toward the northeast and describe initially reverse-dextral displacement that changes to become mainly strike-slip, resulting in a convex-down geometry consistent with our model (Figure 11b).

3.2.3. 2010 M_w 7.2 El Mayor-Cucapah, Baja California

This event nucleated in the center of what would become a 120 km long northwest-southeast oriented bilateral rupture on the border between United States and Mexico. Northwest of the hypocenter, surface rupture extended ~60 km along several northeast-dipping oblique strike-slip-normal faults in the Sierra Cucapah Mountains, with surface slip magnitudes reaching 3–4 m (Fletcher et al., 2014; Wei et al., 2011). The focal mechanism reported in Wei et al. (2011) shows pure dextral strike-slip with a rake close to −180° for this part of the earthquake sequence. Southeast of the hypocenter, rupture propagated ~60 km across the Colorado River delta, where it produced minimal and discontinuous surface rupture (Fletcher et al., 2014; Wei et al., 2011).

Curved slickenlines were documented 16 km northwest of the hypocenter on a northeast-facing scarp of the Pescadores fault—the most structurally simple part of this earthquake rupture (Figures 9c and 10c) (Fletcher et al., 2014). Here surface slip magnitudes were 3.4 m dextral and 0.65 m vertical (hanging wall downthrown). Curved slickenlines ~1.2 m long can be seen on the lower portion of the scarp, which have a convex-down geometry, consistent with our model (Figure 11b).

3.2.4. 1995 M_w 7.0 Neftegorsk, Sakhalin Island

The Neftegorsk earthquake produced a 35 km long, north-trending surface rupture on the steeply dipping strike-slip Upper Pil'tun fault (Shimamoto, 1996) (Figures 9d and 10d). The epicenter was located ~5 km south of the southern tip of surface break, and rupture propagated exclusively toward the northeast (Katsumata et al., 2014). The focal mechanism of this event is close to pure strike-slip with a rake angle of −178° (United States Geological Survey [USGS] catalogue). The average dextral displacement at the surface trace was 3.8 m while vertical slip was mostly less than 1 m (Shimamoto, 1996).

Eight kilometers north of the southern tip of the rupture trace, linear slickenlines pitching ~45° to the southwest were documented on a ~1 m high, southeast-facing vertical free face (Shimamoto, 1996). These observations suggest that the corresponding lateral slip at this site would also have been ~1 m; however, piercing points record dextral displacement of 3.8–4.4 m. As such, the direction of coseismic slip must have

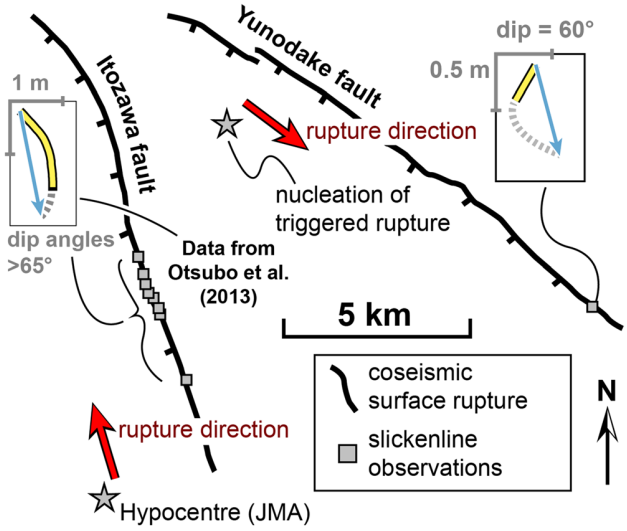

Figure 8. Map of surface faulting and direction of rupture propagation associated with the 2011 M_w 6.6 Fukushima earthquake, Japan. Surface rupture traces are from Mizoguchi et al. (2012). Inferred directions of rupture propagation (red arrows) on each fault are from Tanaka et al. (2014).

changed during the rupture. As there were no horizontal striae observed on this scarp, we infer the following evolution of slip at this site: initially, slip was parallel to the observed slickenlines and was characterized by near equal amounts of strike-slip and dip-slip, producing a scarp close to 1 m high (Figure 10d). Later, the direction of slip changed to become nearly pure strike-slip, and the remaining ~3 m of dextral displacement was accomplished (Figures 9d and 10d). The part of the fault plane that was exposed during the initial stage of slip would be unable to record later strike-slip motion, as it would no longer be in contact with the other side of the fault. As such, any striae formed during this latter, strike-slip part of the rupture would be concealed on the fault plane beneath the ground surface. The curve of this slip path is convex-down and is consistent with our model (Figure 11b).

3.2.5. 1954 M_w 7.1 Fairview Peak, United States

The Fairview Peak earthquake produced surface faulting on several east-dipping normal faults within the Basin and Range, including 32 km of rupture on the Fairview fault (Caskey et al., 1996; Slemmons, 1957). The earthquake nucleated at 12-km depth near the center of the Fairview fault and ruptured bilaterally, extending ~18 km to the southwest and ~14 km to the northeast (Figures 9e and 10e). The focal mechanism for this earthquake represents normal-dextral slip with a rake of −160° (Doser, 1986). Surface offsets showed a significant component of normal slip, with peak vertical displacements of 3.6 m (Caskey et al., 1996; Slemmons, 1957). In his post-earthquake geological report, Slemmons (1957) noted that slickenlines on free faces of the Fairview fault showed lower rake angles near the top of the scarp and steeper rake angles near the base, suggesting that "... the waning moments of movement were characterised by more nearly dip-slip components of movement."

Furthermore, he provides quantitative details from a location where he observed considerable discrepancy between the rake angle of slickenlines (yellow line in Figures 9e and 10e) and the overall direction of coseismic displacement recorded by piercing points at the same site (blue vector is Figures 9e and 10e). These observations both support the interpretation that slip started out as normal-dextral strike-slip and later in the rupture changed direction to include an increasing component of dip slip. The convexity of the slip path is convex-up and is consistent with our model (Figure 11c).

3.2.6. 1988 M_s 6.9 Spitak, Armenia

The Spitak, Armenia, earthquake produced a discontinuous surface rupture trace along the northeast-dipping Alavar reverse fault (Philip et al., 1992). The most prominent surface break was characterized by a continuous, 10 km long and ~1 m high reverse fault scarp with its southeast tip located near the town of Spitak (Dorbath et al., 1992). The earthquake nucleated at 5-km depth near Spitak and propagated bilaterally, with peak surface displacement (1.6 m vertical, 0.9 m dextral) located to the northwest of the hypocenter in the middle of the 10 km long rupture segment (Figures 9f and 10f) (Dorbath et al., 1992).

At the site of maximum surface slip, the rupture trace consisted of an overhanging free face decorated with slickenlines (Figures 9f and 10f) (Avagyan et al., 2003). Two main sets of linear slickenlines were observed to overlap one another, each raking at ~45° in opposite directions. These two sets of striae described initial sinistral-reverse, followed by dextral-reverse displacement during the earthquake (Avagyan et al., 2003). The authors interpreted these observations as the results of two separate rupture fronts (during the single M_s 6.9 earthquake), each with different slip directions. However, we suggest that these two sets could have been formed during a single slip episode (Figure 9f). Under this interpretation, the convexity of the curved slip path is toward the hypocenter and is consistent with our model (Figure 11c).

3.2.7. 2016 M_w 7.8 Kaikōura, New Zealand

This event produced surface fault rupture on >20 faults in the northeast of South Island, New Zealand (Hamling et al., 2017; Litchfield et al., 2018). Despite the complex pattern of surface rupture, the rupture propagation was dominantly unilateral; the earthquake propagated northeast for ~200 km (Ando &

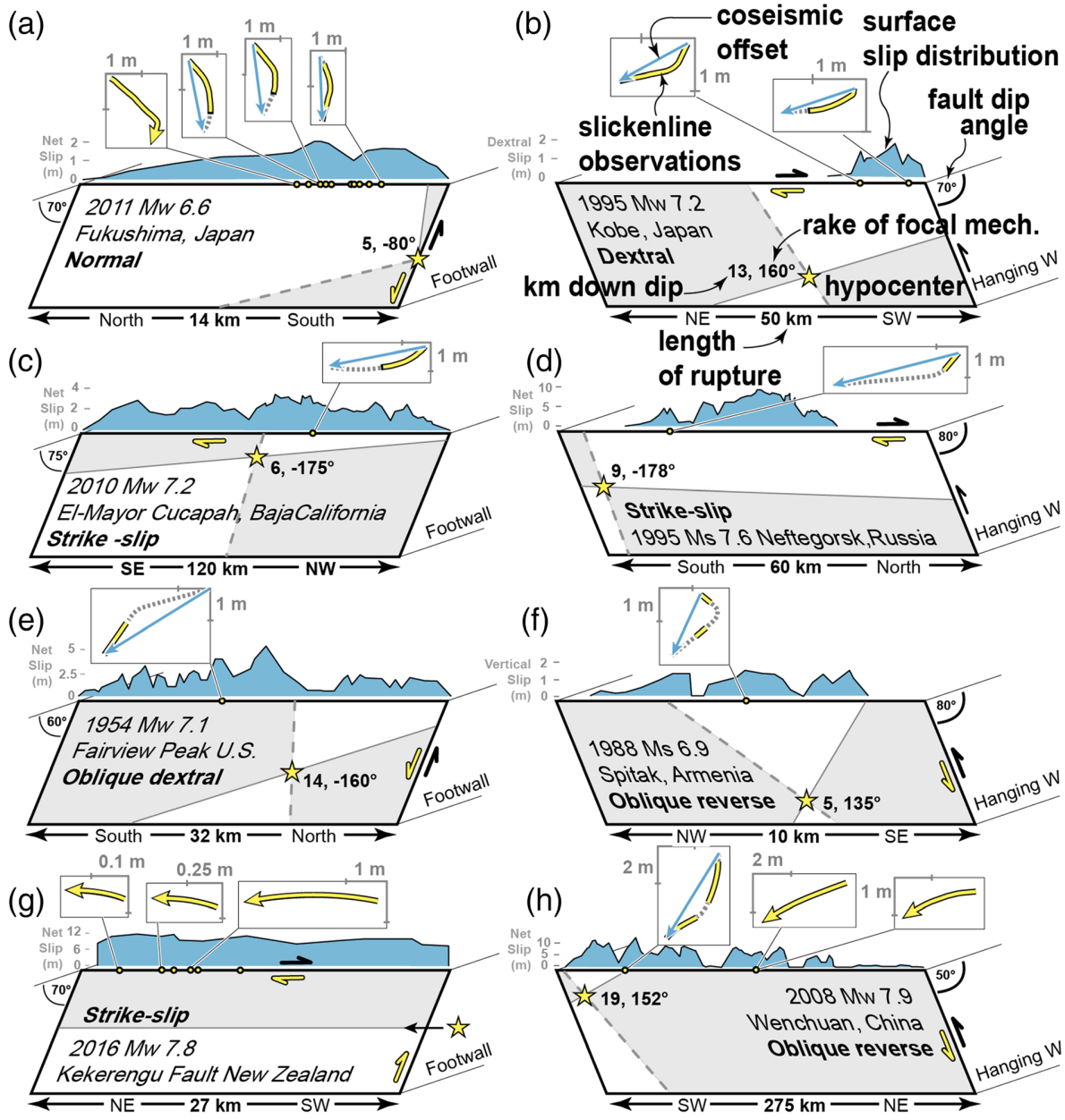

Figure 9. Comparison of earthquake data and model framework. Mixed-mode quadrants (gray and white) on fault planes are separated by mode II (solid gray line) and mode III rupture directions (dashed gray line). Blue slip vectors adjacent to slickenline data represent piercing point offsets at each corresponding site. (a) 2011 M_w 6.6 Fukushima earthquake, Japan (Mizoguchi et al., 2012; Otsubo, Shigematsu, et al., 2013). (b) 1995 M_w 7.2 Kobe earthquake, Japan (Otsuki et al., 1997; Spudich et al., 1998). (c) 2010 M_w 7.2 El-Mayor Cucapah earthquake, Baja California (Fletcher et al., 2014). (d) 1995 M_s 7.6 Neftegorsk earthquake, Russia (Shimamoto, 1996). (e) 1954 M_w 7.1 Fairview Peak earthquake, Nevada (Caskey et al., 1996; Slemmons, 1957). (f) 1988 M_s 6.9 Spitak earthquake, Armenia (Avagyan et al., 2003; Philip et al., 1992). (g) 2016 M_w 7.8 Kaikōura earthquake, New Zealand (Kearse et al., 2018). Coseismic net slip data for this earthquake are not shown due to the scale of the offsets. For simplicity, we only show the Kekerengu fault. Rupture propagated from southwest to northeast. (h) 2008 M_w 7.9 Wenchuan earthquake, China (Pan et al., 2014; Perrin et al., 2016). We were unable to obtain coseismic net slip data for the northern two sites.

Kaneko, 2018; Kaiser et al., 2017) and produced large dextral displacements of up to 12 m on the Kekerengu fault located near the northeast tip of the rupture (Kearse et al., 2018).

Curved slickenlines were observed (Kearse et al., 2019) at multiple sites on the Kekerengu fault (Figures 9g and 10g). These slickenlines described a curved slip path, whereby the displacement was initially

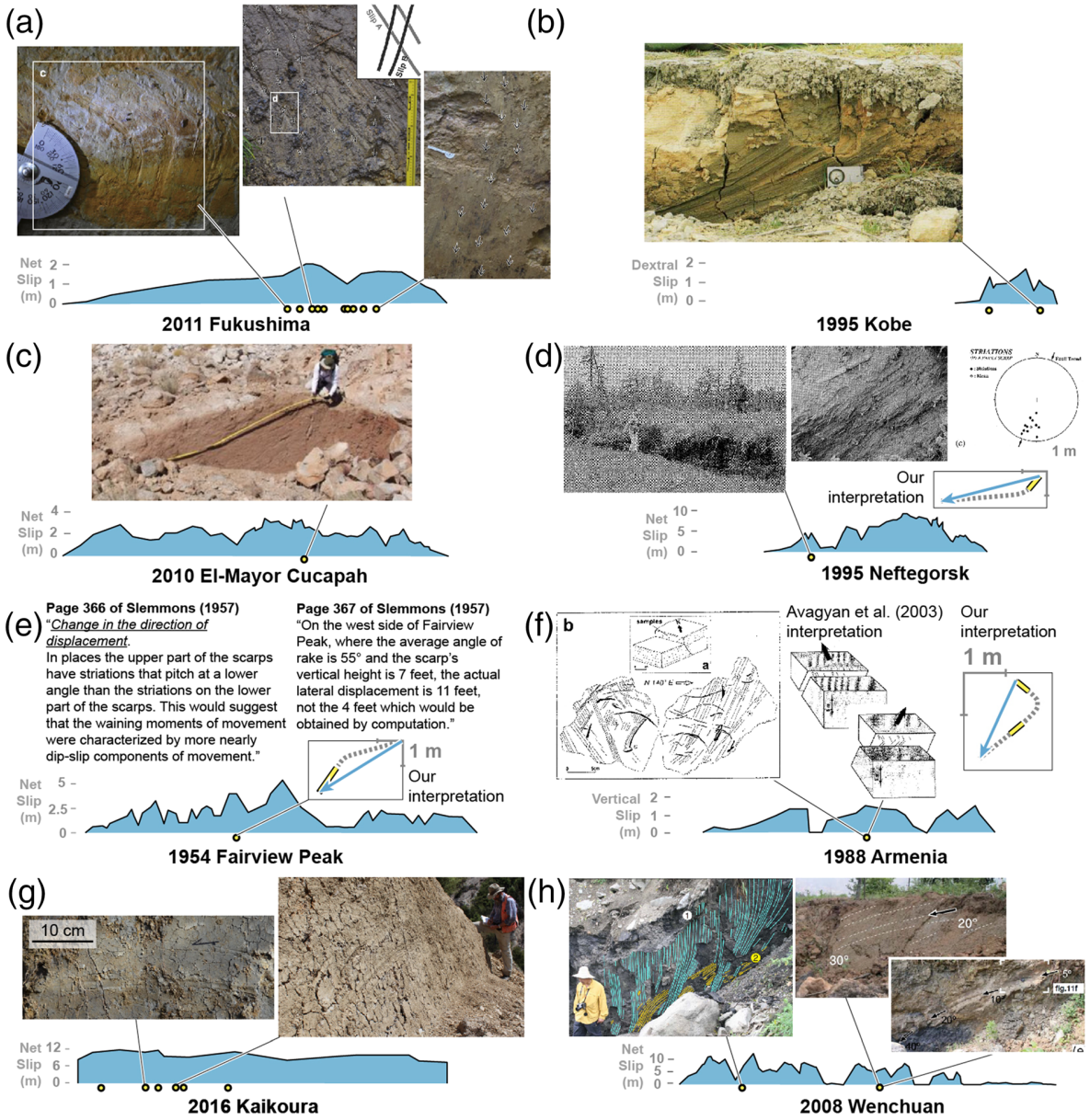

Figure 10. Examples of coseismic changes in slip direction used in this study. Blue slip vectors adjacent to slickenline data represent piercing point offsets. (a) 2011 M_w 6.6 Fukushima earthquake, Japan (Otsubo, Shigematsu, et al., 2013). (b) 1995 M_w 7.2 Kobe earthquake, Japan (Otsuki et al., 1997). (c) 2010 M_w 7.2 El Mayor-Cucapah earthquake, Baja California (Fletcher et al., 2014). (d) 1995 M_s 7.6 Neftegorsk earthquake, Russia (Shimamoto, 1996). (e) 1954 M_w 7.1 Fairview Peak earthquake, Nevada (Slemmons, 1957). (f) 1988 M_s 6.9 Spitak earthquake, Armenia (Avagyan et al., 2003). (g) 2016 M_w 7.8 Kaikoura earthquake, New Zealand (Kearse et al., 2018, 2019). For this event, we are showing the length of the Kekerengu fault. (h) 2008 M_w 7.9 Wenchuan earthquake, China (Pan et al., 2014).

reverse-dextral and later transitioned to become nearly pure strike-slip, describing a convex-up geometry that is consistent with our model (Figure 11b). At two locations on the Kekerengu fault, slickenlines with a convex-down geometry were observed. However, these two locations were associated with sharp bends in the surface rupture trace and reversals in the sense of throw on the fault, suggesting that these structural complexities overwhelmed the dynamic effects discussed here (Kearse et al., 2019).

3.2.8. 2008 M_w 7.9 Wenchuan, China

The Wenchuan earthquake initiated near the town of Yingxiu and ruptured unilaterally toward the northeast, generating ~230 km of surface rupture (Xu et al., 2009). Slip measured at the surface trace shows

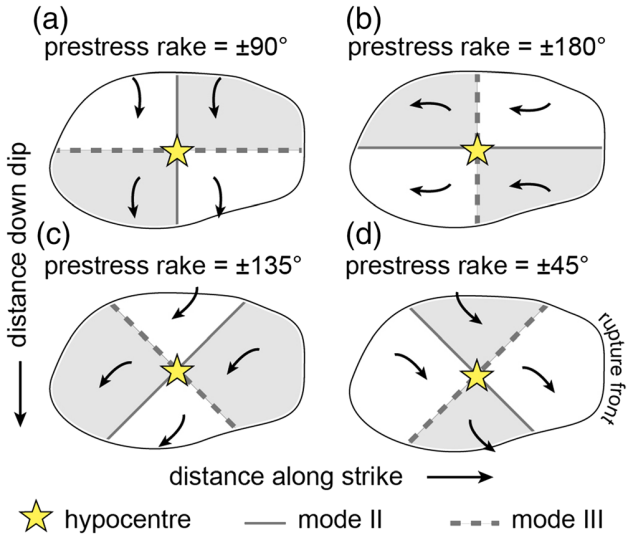

Figure 11. Spatial pattern of curved slickenlines resulting from various rake angles of prestress. In each case shown in this figure, negative rake angles correspond to a fault plane view that looks toward the footwall, while positive rake angles correspond to a fault plane view toward the hanging wall. (a) Normal or reverse rupture with pure dip-slip prestress rake angles. (b) Pure strike-slip faulting, either dextral (180°) or sinistral (0°). (c) Dextral-normal (negative angles) or dextral-reverse (positive angles) rupture. (d) Sinistal-normal (negative angles) or sinistral-reverse rupture (positive angles).

considerable variation along strike: dextral-reverse near the epicenter and mainly dextral toward the northeast (Xu et al., 2009).

Curved slickenlines were observed at two locations: ~40 km along strike from the hypocenter near Bajiaomiao and ~150 km along strike from the hypocenter at Beichuan (Pan et al., 2014) (Figures 9h and 10h). The surface rupture trace near the Bajiaomiao site is structurally complex. This site is located between a bifurcation of the Yingxiu-Beichuan fault to the south and a 90° "T" junction with the oblique sinistral Xiaoyudong fault <5 km to the north (Pan et al., 2014). Here, two overlapping sets of curved slickenlines were observed. One set (generated first, according to the detailed interpretation of Pan et al., 2014) is convex-down and steeply pitching (70–80°), and the other (generated later) is moderately pitching (30–50°) with a convex-up geometry (Figures 9h and 10h). At the Beichuan site, the surface rupture trace is structurally simple. Multiple exposures of curved slickenlines are observed here and all show the same geometry. Slickenlines initially pitch 10–30° to the southwest and then steepen to ~50°, describing a convex-up slip path similar to the second set of slickenlines seen at Bajiaomiao, and which are consistent with our model (Figure 11c).

4. Discussion and Conclusions

The correlation between our models and the historical observations exposes an underlying simplicity within the available earthquake data despite the apparently complex geometries of documented slickenlines. The sense of slickenline convexities is determined by the location and rake of their earthquake source mechanism and is generated by dynamic stresses within the process zone of the propagating rupture (Figures 6 and 9). It follows therefore that on-fault, geological observations of this type can be used to reveal the direction of rupture propagation.

4.1. Unearthing Slickenlines

In practice, to identify rupture direction from curved slickenlines would require observations at one or more sites along the surface trace of a fault that has sustained a ground rupturing earthquake in the past. Subaerially exposed slickenlines (i.e., those seen on exposed fault plane surfaces) formed within soft fault gouge are generally ephemeral features; fault trenching to expose fresh slip surfaces at shallow depth is therefore likely to provide the most useful data, especially if the fault under investigation has not ruptured the surface for decades or more. Traditionally, earthquake trenching efforts have focused on sites likely to record young and delicate sequences of soft, organic-rich sediment that can be easily dated. For the purposes of uncovering slickenlines, however, site selection should follow different criteria. We suggest that mature fault surfaces within bedrock are better targets, as they are more likely to contain the abrasive conditions necessary for slickenline generation and preservation. In addition, structurally simple parts of active faults should be prioritized, as distinct changes in slip direction have been found near complexities in surface ruptures (e.g., Kearse et al., 2019; Pan et al., 2014).

To expose up to several square meters of fault plane surface, we propose a different style of excavation than is typical of trenches with a paleoseismicity focus. Initially, a small pilot trench would be incised across the target fault scarp to constrain the location and orientation of the fault plane in cross section (Figures 12a and 12b). Next, a fault-parallel trench located on one side of the fault would be incised to remove the bulk of material adjacent to the fault surface (Figure 12c). It is critical that the trenching process does not destroy or modify in any way the condition of the buried fault surface. Thus, we suggest that excavation by machinery is stopped short of exposing the fault plane (e.g., Figure 12c). As the final stage, the fault plane should be carefully uncovered by hand, so as not to introduce any artificial slickenlines (Figure 12d). In a successful attempt at unearthing coseismic slickenlines on a buried fault plane, Otsubo, Miyashita, et al. (2013) excavated a trench subparallel to the 2011 rupture trace of the Yunodake fault.

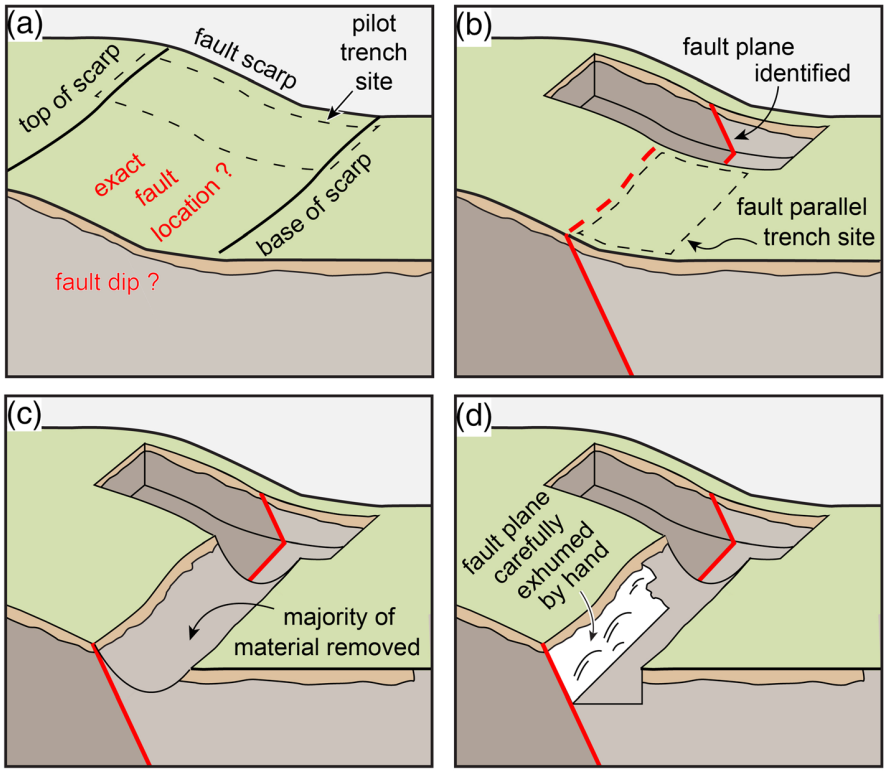

Figure 12. Cartoon of proposed trench excavation process. (a) Uncertainty in fault plane location. Dashed box outlines location of proposed pilot trench. (b) Fault plane identification following pilot trench excavation. Dashed box outlines adjacent site for fault-parallel trench. (c) Removal of material from next to the fault plane. We propose that this be done using machinery, with care taken to avoid disturbing the fault surface. (d) Last stage is carefully removing material by hand to expose the fault plane surface.

Due to the destructive ploughing process during slickenline formation in soft fault gouge, it is unlikely that any discrete slip surface will preserve slickenlines older than its most recent slip episode. In post-earthquake field investigations, slickenlines are commonly inscribed onto extremely fragile fault gouge, exhibit sharp micro-topographic relief across their tracks (e.g., Figure 13a), and therefore can be confidently attributed to the most recent earthquake (Spudich et al., 1998; Kearse et al., 2018, 2019). Using these criteria, overlapping slickenlines, each with different slip directions, documented in these post-earthquake scenarios have been interpreted as forming in the same slip episode involving coseismic changes in slip direction (Kearse et al., 2018, 2019; Otsubo, Shigematsu, et al., 2013; Pan et al., 2014) (e.g., Figure 13b). Relict slip planes adjacent to principle slip surfaces have been found to host slickenlines that appear much older than the most recent earthquake (e.g., Figure 13c), suggesting that there is potential for preserving slickenlines from more than one earthquake event, within a fault zone at a single location. However, assigning an absolute age to any particular slickenline (except those assigned to the most recent earthquake) may not yet be possible with current dating techniques. Therefore, when exhuming a paleoslip surface on an active fault, it is likely that the rupture direction of only the most recent earthquake can be determined using this new method.

4.2. Slickensides and Linear Slickenlines

The widespread occurrence of dynamic changes in slip direction raises questions about the processes responsible for the generation of linear slickenlines formed in surface rupturing earthquakes. Typically, slickenlines only record a fraction of coseismic slip (Avagyan et al., 2003; Kearse et al., 2018; Lin et al., 2002) and therefore may only represent a short, linear part of a longer curved slip path (Shimamoto, 1996). Alternatively, they may be part of an entirely linear slip path that formed along a mode II or mode III

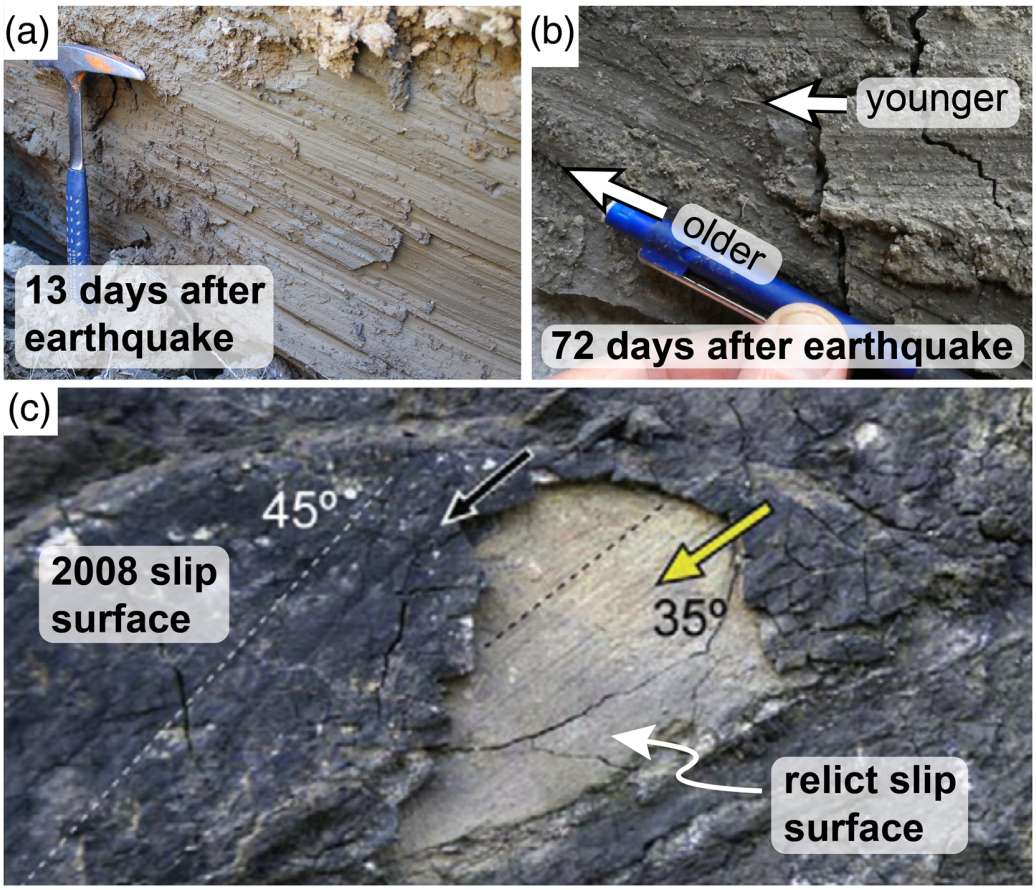

Figure 13. Slickenlines of various ages. (a, b) Slickenlines observed on the Kekerengu fault after the Kaikoura earthquake. Note the fresh and delicate nature of the gouge-covered surface shown in (a). Photo taken 13 days after the earthquake by Kate Clark (GNS Science); geological hammer for scale. (b) Overlapping slickenlines in extremely delicate gouge, both formed during 2016 Kaikoura earthquake. Photo taken 72 days after the earthquake by Jesse Kearse; pen for scale. (c) Slickenlines observed on the Beichuan fault after the 2008 Wenchuan earthquake (photo taken from Pan et al., 2014). In the center of the photograph, a patch of the 2008 slip surface has been eroded to expose a relict slip surface; scale unknown.

rupture, such as those found above the hypocenter of the 1999 M_w 7.1 strike-slip Hector Mine earthquake (Treiman et al., 2002).

It is important to recognize that slip directions defined by linear slickenlines inscribed on a fault plane surface may not necessarily represent the overall kinematics of that fault. For example, linear slickenlines were observed on a fresh free face of the Yunodake fault following the 2011 M_w 6.6 Fukushima earthquake (Figure S1). If taken at face value, the slip direction defined by these slickenlines suggests dextral-normal slip at a pitch of 60° north (Figure S1). Yet the true 3D slip vector for this site during the 2011 earthquake is orientated at a pitch of ~75° south, a difference of 45° in the plane of the fault.

Geologists have long observed and measured slickenlines on exposed long-term fault planes (Doblas, 1998; Petit, 1987; Twiss et al., 1991). These so-called slickensides are hard, reflective fault surfaces that generally contain well-developed slip-parallel corrugations whose spatial dimensions are self-similar (Candela et al., 2012; Renard et al., 2013). Observations of natural faults and results of laboratory shearing experiments suggest that slickenlines of this type are formed through both brittle and ductile processes (Kuo et al., 2016; Power & Tullis, 1989; Toy et al., 2017) and smooth the fault surface in the direction of slip (Brodsky et al., 2011). The depth at which these surfaces form is not well constrained, but there is evidence to suggest that they can form in the upper 5 km (e.g., Kirkpatrick et al., 2013; Power & Tullis, 1989). The strong

linearity of grooves preserved on the surfaces of many slickenside outcrops, such as the Corona Heights fault in California (Kirkpatrick et al., 2013; Kirkpatrick & Brodsky, 2014) and the Dixie Valley fault in Nevada (Candela & Renard, 2012; Power & Tullis, 1989), appears to be at odds with the findings of this study. These discrepancies, however, may reflect differences in coseismic slip direction on the fault at the ground surface (focus of this paper) and on the fault at depth. For example, our dynamic models predict increasing suppression of coseismic slip curvature with depth, with less than 2° of curvature at 4-km depth. There is also likely to be greater resistance to changes in slip direction than is captured in our model (based on a planar fault and isotropic friction); pronounced slip-parallel corrugations on the fault interface are thought to create significant stress anisotropy (e.g., Power et al., 1987; Toy et al., 2017), making it more difficult for dynamic stresses to drive coseismic changes in slip direction.

Slickensides of this type are brought to the surface either through fault slip or exhumation (or both) and retain their hard, reflective character making them resistant to erosion. Slickenlines generated at the ground surface are generally imbedded within soft fault gouge or clay and do not withstand subaerial weathering. They can also form as shallow scratches on hard slickenside surfaces, such as those formed during the 2016 Central Italy earthquake sequence (Pucci et al., 2017; Villani et al., 2018), and are not necessarily colinear with the inherited slickenside fabric (e.g., Galderesi & Galli, 2020).

4.3. Limitations and Future Work

Heterogeneity in fault structure or stress, including those arising from lateral variation in fault maturity, is known to influence the dynamics of earthquake rupture (Dunham et al., 2011; Harris & Day, 1999; Perrin et al., 2016; Ripperger et al., 2007) and could complicate the predicted patterns of slip-path convexity. Such fault behavior was seen following the 2016 Kaikoura earthquake, where distinct changes in slip direction were observed at sharp fault bends and step overs (Kearse et al., 2019; Pan et al., 2014). The reasons for this distinct slip behavior are not yet clear, and investigation of rupture direction using curved slickenlines should focus on structurally simple parts of active faults—that is, parts which are straight and aligned parallel to the average strike of the fault and which contain only one strand.

Although supershear rupture propagation is present in our models (e.g., Hu et al., 2019; Kaneko & Lapusta, 2010), it does not become a dominant instability and thus has little effect on slip behavior or temporal changes in slip direction. Cases in which free-surface-induced supershear rupture propagation becomes dominant may influence temporal changes in slip direction and may even lead to observable phase transitions preserved in slickenlines tracks. This remains a subject of future work.

4.4. Implications for Seismology

Our theoretical framework for interpreting curved slickenlines (Figure 1) will enable earthquake geologists to determine the rupture propagation directions of earthquakes lacking instrumental data. One famous example of a large earthquake with a poorly constrained rupture direction is the 1857 M_w 7.9 Fort Tejon earthquake in southern California (Harris & Simpson, 1996; Sieh, 1978a). It has been suggested that this 360 km long rupture propagated southeastward (Sieh, 1978b); however, there are no instrumental data associated with this earthquake, and an opposite (or bilateral) direction of rupture propagation cannot be ruled out. Our results suggest that trenching the 1857 section of the San Andreas fault in pursuit of curved slickenlines could constrain the rupture direction of this earthquake, which underpins realistic earthquake simulation exercises and the assessment of ground motion hazard in earthquake-prone regions (Bielak et al., 2010; Bouchon & Aki, 1980).

Another potential application of this research is to constrain the rupture pathway of complex earthquakes. For instance, important details of the propagating rupture pathway of the 2016 M_w 7.8 Kaikōura earthquake remain unresolved due to sparse instrumental coverage (Ando & Kaneko, 2018; Hamling et al., 2017; Klinger et al., 2018; Litchfield et al., 2018; Ulrich et al., 2019). Independent, on-fault evidence of rupture direction—such as curved slickenlines—would place strong constraints on which rupture scenarios are most valid, providing critical insight into how dynamic rupture can navigate crustal fault networks to produce complex earthquakes.

Some theoretical studies (Andrews & Ben-Zion, 1997) have shown that rupture propagation direction should be influenced by elastic contrasts across bi-material faults, while other research (Harris & Day, 2005) has presented both empirical and numerical evidence suggesting that there is no preferred rupture direction.

Debate surrounding this topic suffers from insufficient observations that constrain the rupture direction of past large earthquakes on mature, plate boundary faults. Our method unifies fault mechanics theory and earthquake physics with historical and recent geological observations of earthquake rupture propagation directions to provide a robust method that earthquake geologists can employ to increase global observations of rupture propagation direction in past large earthquakes.

Data Availability Statement

The data on which this article is based can be found within Avagyan et al. (2003), Caskey et al. (1996), Fletcher et al. (2014), Kearse et al. (2018, 2019), Mizoguchi et al. (2012), Otsubo, Shigematsu, et al. (2013), Otsuki et al. (1997), Pan et al. (2014), Perrin et al. (2016), Philip et al. (1992), Shimamoto (1996), Slemmons (1957), and Spudich et al. (1998).

Acknowledgments
The authors acknowledge Tim Little, Russ Van Dissen, Carolyn Boulton, John Townend, and Laura Wallace for useful discussion that significantly improved the manuscript. We thank editor Isabelle Manighetti, associate editor Alice Gabriel, and reviewers Hongfeng Yang and Nicholas Barth for their comments that helped us improve the manuscript. We thank Kazuo Mizoguchi for providing key information and photographs on the Yunodake Fault surface rupture. This study was supported by Rutherford Discovery Fellowship from the Royal Society of New Zealand and the New Zealand eScience Infrastructure (NeSI) high-performance computing facilities.

References

Ampuero, J. P. (2002). Etude physique et numérique de la nucléation des séismes: PhD Thesis, *University of Paris VII, France*.

Ando, R., & Kaneko, Y. (2018). Dynamic rupture simulation reproduces spontaneous multifault rupture and arrest during the 2016 M_w 7.9 Kaikoura earthquake. *Geophysical Research Letters*, *45*, 12,875–12,883. https://doi.org/10.1029/2018GL080550

Andrews, D. J. (1994). Dynamic growth of mixed-mode shear cracks. *Bulletin of the Seismological Society of America*, *84*, 1184–1198.

Andrews, D. J., & Ben-Zion, Y. (1997). Wrinkle-like slip pulse on a fault between different materials. *Journal of Geophysical Research*, *102*(B1), 553–571. https://doi.org/10.1029/96JB02856

Arrowsmith, R., & Rhodes, D. D. (1994). Original forms and initial modifications of the Galway Lake Road scarp formed along the Emerson fault during the 28 June 1992 Landers, California, earthquake. *Bulletin of the Seismological Society of America*, *84*(3), 511–527. https://pubs.geoscienceworld.org/ssa/bssa/article/84/3/511/102580?casa_token=8O-G3sALp50AAAAA:mlB1Uv-stkOpH1tfm_32h6Qo9PpQ9VaHQ3IZfda5oj4dPqwPbRRvukEzKfnCJwMppvWe81t5TKA

Avagyan, A., Ritz, J. F., Karakhanian, A., & Philip, H. (2003). Dual near-surface rupturing mechanism during the 1988 Spitak earthquake (Armenia). *National Academy of Sciences of the Republic of Armenia*, *56*, 14–19.

Barbot, S., Lapusta, N., & Avouac, J. P. (2012). Under the hood of the earthquake machine: Toward predictive modeling of the seismic cycle. *Science*, *336*(6082), 707–710. https://doi.org/10.1126/science.1218796

Bielak, J., Graves, R. W., Olsen, K. B., Taborda, R., Ramírez-Guzmán, L., Day, S. M., et al. (2010). The ShakeOut earthquake scenario: Verification of three simulation sets. *Geophysical Journal International*, *180*(1), 375–404. https://doi.org/10.1111/j.1365-246X.2009.04417.x

Bizzarri, A., & Cocco, M. (2003). Slip-weakening behavior during the propagation of dynamic ruptures obeying rate- and state-dependent friction laws. *Journal of Geophysical Research*, *108*(B8), 2373. https://doi.org/10.1029/2002JB002198

Bouchon, M., & Aki, K. (1980). Simulation of long-period, near-field motion for the great California earthquake of 1857. *Bulletin of the Seismological Society of America*, *70*, 1669–1682.

Brodsky, E. E., Gilchrist, J. J., Sagy, A., & Collettini, C. (2011). Faults smooth gradually as a function of slip. *Earth and Planetary Science Letters*, *302*(1–2), 185–193. https://doi.org/10.1016/j.epsl.2010.12.010

Candela, T., & Renard, F. (2012). Segment linkage process at the origin of slip roughness: Evidence from the Dixie Valley fault. *Journal of Structural Geology*, *45*, 87–100. https://doi.org/10.1016/j.jsg.2012.06.003

Candela, T., Renard, F., Klinger, Y., Mair, K., Schmittbuhl, J., & Brodsky, E. E. (2012). Roughness of fault surfaces over nine decades of length scales. *Journal of Geophysical Research*, *117*, B08409. https://doi.org/10.1029/2011JB009041

Caskey, S. J., Wesnousky, S. G., Zhang, P., & Slemmons, D. B. (1996). Surface faulting of the 1954 Fairview Peak (M_s 7.2) and Dixie Valley (M_s 6.8) earthquakes, Central Nevada. *Bulletin of the Seismological Society of America*, *86*, 761–787.

Crone, A. J., Machette, M. N., Bonilla, M. G., Lienkaemper, J. J., Pierce, K. L., Scott, W. E., & Bucknam, R. C. (1987). Surface faulting accompanying the Borah Peak earthquake and segmentation of the lost river fault, central Idaho. *Bulletin of the Seismological Society of America*, *77*(2), 739–770. https://pubs.geoscienceworld.org/ssa/bssa/article/77/3/739/118922?casa_token=Jb0bVjYo2rcAAAAA:gCQbCoJhWBqX0FnCwQ3JtgsURdRce2EuA6Wi0Vjn1GyxVemZBrRpYxpXiZuuXMuTn2CV4ok-_8E

Crone, A. J., Machette, M. N., & Bowman, J. R. (1992). Geologica investigations of the 1988 Tennant Creek, Australia, earthquakes; implications for paleoseismicity in stable continental regions. *U.S. Geological Survey Bulletin 2032-A*. https://doi.org/10.3133/b2032A

Doblas, M. (1998). Slickenside kinematic indicators. *Tectonophysics*, *295*(1–2), 187–197. https://doi.org/10.1016/S0040-1951(98)00120-6

Dorbath, L., Dorbath, C., Rivera, L., Fuenzalida, A., Cisternas, A., Tatevossian, R., et al. (1992). Geometry, segmentation and stress regime of the Spitak (Armenia) earthquake from the analysis of the aftershock sequence. *Geophysical Journal International*, *108*(1), 309–328. https://doi.org/10.1111/j.1365-246X.1992.tb00860.x

Doser, D. I. (1986). Earthquake processes in the Rainbow Mountain-Fairview Peak-Dixie Valley, Nevada, region 1954–1959. *Journal of Geophysical Research*, *91*(B12), 12,572–12,586. https://doi.org/10.1029/JB091iB12p12572

Dunham, E. M., Belanger, D., Cong, L., & Kozdon, J. E. (2011). Earthquake ruptures with strongly rate-weakening friction and off-fault plasticity, part 2: Nonplanar faults. *Bulletin of the Seismological Society of America*, *101*(5), 2308–2322. https://doi.org/10.1785/0120100076

Fletcher, J. M., Teran, O. J., Rockwell, T. K., Oskin, M. E., Hudnut, K. W., Mueller, K. J., et al. (2014). Assembly of a large earthquake from a complex fault system: Surface rupture kinematics of the 4 April 2010 El Mayor-Cucapah (Mexico) M_w 7.2 earthquake. *Geosphere*, *10*(4), 797–827. https://doi.org/10.1130/GES00933.1

Florensov, N. A., & Solonenko, V. P. (1965). The Gobi-Altai Earthquake, Springfield, VA: U.S. Dept. of Commerce. https://scholar.google.com/scholar?q%3DThe%20Gobi-Altai%20Earthquake%2C%20Academy%20of%20Sciences%20of%20the%20USSR%26author%3DN.%20A.%20Florensov%26author%3DV.%20P.%20Solonenko%26publication_year%3D(1965)%26book%3D

Galderesi, A., & Galli, P. (2020). Offset components and fault-block motion during the 2016 Central Italy earthquake (M_w 6.6, Monte Vettore fault system). *Journal of Structural Geology*, *134*, 104014. https://doi.org/10.1016/j.jsg.2020.104014

Gerstenberger, M. C., Marzocchi, W., Allen, T., Pagani, M., Adams, J., Danciu, L., et al. (2020). Probabilistic seismic hazard analysis at regional and national scales: State of the art and future challenges. *Reviews of Geophysics*, *58*, e2019RG000653. https://doi.org/10.1029/2019RG000653

Guatteri, M., & Spudich, P. (1998). Coseismic temporal changes of slip direction: The effect of absolute stress on dynamic rupture. *Bulletin of the Seismological Society of America*, *88*, 777–789.

Guo, J., Lin, A., Sun, G., & Zheng, J. (2007). Surface Ruptures Associated with the 1937 M 7.5 Tuosuo Lake and the 1963 M 7.0 Alake Lake Earthquakes and the Paleoseismicity along the Tuosuo Lake Segment of the Kunlun Fault, Northern Tibet. *Bulletin of the Seismological Society of America*, *97*(2), 474–496. https://doi.org/10.1785/0120050103

Haeussler, P. J., Schwartz, D. P., Dawson, T. E., Stenner, H. D., Lienkaemper, J. J., Sherrod, B., et al. (2004). Surface Rupture and Slip Distribution of the Denali and Totschunda Faults in the 3 November 2002 M 7.9 Earthquake, Alaska. *Bulletin of the Seismological Society of America*, *94*(6B), S23–S52. https://doi.org/10.1785/0120040626

Hamling, I. J., Hreinsdóttir, S., Clark, K., Elliott, J., Liang, C., Fielding, E., et al. (2017). Complex multifault rupture during the 2016 M_w 7.8 Kaikōura earthquake, New Zealand. *Science*, *356*, eaam7194. https://doi.org/10.1126/science.aam7194

Harris, R. A., & Day, S. M. (1999). Dynamic 3D simulations of earthquakes on en echelon faults. *Geophysical Research Letters*, *26*(14), 2089–2092. https://doi.org/10.1029/1999GL900377

Harris, R. A., Barall, M., Aagaard, B., Ma, S., Roten, D., Olsen, K., et al. (2018). A suite of exercises for verifying dynamic earthquake rupture codes. *Seismological Research Letters*, *89*(3), 1146–1162. https://doi.org/10.1785/0220170222

Harris, R. A., Barall, M., Archuleta, R., Dunham, E., Aagaard, B., Ampuero, J. P., et al. (2009). The SCEC/USGS dynamic earthquake rupture code verification exercise. *Seismological Research Letters*, *80*(1), 119–126. https://doi.org/10.1785/gssrl.80.1.119

Harris, R. A., & Day, S. M. (2005). Material contrast does not predict earthquake rupture propagation direction. *Geophysical Research Letters*, *32*, L23301. https://doi.org/10.1029/2005GL023941

Harris, R. A., & Simpson, R. W. (1996). In the shadow of 1857—The effect of the great Ft. Tejon earthquake on subsequent earthquakes in southern California. *Geophysical Research Letters*, *23*(3), 229–232. https://doi.org/10.1029/96GL00015

Hu, F., Oglesby, D. D., & Chen, X. (2019). The sustainability of free-surface-induced supershear rupture on strike-slip faults. *Geophysical Research Letters*, *46*, 9537–9543. https://doi.org/10.1029/2019GL084318

Ida, Y. (1972). Cohesive force across the tip of a longitudinal-shear crack and Griffith's specific surface energy. *Journal of Geophysical Research*, *77*(20), 3796–3805. https://doi.org/10.1029/JB077i020p03796

Jones, C. (1915). The pleasant valley, Nevada, earthquake of October 2, 1915. *Bulletin of the Seismological Society of America*, *5*(4), 190–205. https://pubs.geoscienceworld.org/bssa/article-lookup/5/4/190

Kaiser, A., Balfour, N., Fry, B., Holden, C., Litchfield, N., Gerstenberger, M., et al. (2017). The 2016 Kaikōura, New Zealand, earthquake: Preliminary seismological report. *Seismological Research Letters*, *88*(3), 727–739. https://doi.org/10.1785/0220170018

Kakimi, T., & Kinugasa, Y. (1977). Geological research on the Izu–Hanto–oki earthquake of 1974. In *Special Report of the Geological Society of Japan*. https://scholar.google.com/scholar?hl=en&as_sdt=0%2C5&q=izu-hanto-oki+earthquake+1974+kakimi&btnG=

Kaneko, Y., & Lapusta, N. (2010). Supershear transition due to a free surface in 3-D simulations of spontaneous dynamic rupture on vertical strike-slip faults. *Tectonophysics*, *493*(3–4), 272–284. https://doi.org/10.1016/j.tecto.2010.06.015

Kaneko, Y., Lapusta, N., & Ampuero, J. P. (2008). Spectral element modeling of spontaneous earthquake rupture on rate and state faults: Effect of velocity-strengthening friction at shallow depths. *Journal of Geophysical Research*, *113*, B09317. https://doi.org/10.1029/2007JB005553

Katsumata, K., Kasahara, M., Ichiyanagi, M., Kikuchi, M., Sen, R. S., Kim, C. U., et al. (2014). The 27 May 1995 M_s 7.6 northern Sakhalin earthquake: An earthquake on an uncertain plate boundary. *Bulletin of the Seismological Society of America*, *94*(1), 117–130. https://doi.org/10.1785/0120020175

Kearse, J., Kaneko, Y., Little, T., & Van Dissen, R. J. (2019). Curved slickenlines preserve the direction of rupture propagation. *Geology*, *47*(9), 838–842. https://doi.org/10.1130/G46563.1

Kearse, J., Little, T. A., Van Dissen, R. J., Barnes, P. M., Langridge, R., Mountjoy, J., et al. (2018). Onshore to offshore ground-surface and seabed rupture of the Jordan-Kekerengu-Needles fault network during the 2016 M_w 7.8 Kaikōura earthquake, New Zealand. *Bulletin of the Seismological Society of America*, *108*(3B), 1573–1595. https://doi.org/10.1785/0120170304

Kirkpatrick, J. D., & Brodsky, E. E. (2014). Slickenline orientations as a record of fault rock rheology. *Earth and Planetary Science Letters*, *408*, 24–34. https://doi.org/10.1016/j.epsl.2014.09.040

Kirkpatrick, J. D., Rowe, C. D., White, J. C., & Brodsky, E. E. (2013). Silica gel formation during fault slip: Evidence from the rock record. *Geology*, *41*, 1015–1018. https://doi.org/10.1130/G34483.1

Klinger, Y., Okubo, K., Vallage, A., Champenois, J., Delorme, A., Rougier, E., et al. (2018). Earthquake damage patterns resolve complex rupture processes. *Geophysical Research Letters*, *45*, 10,279–10,287. https://doi.org/10.1029/2018GL078842

Kuo, L.-W., Song, S.-R., Suppe, J., & Yeh, E.-C. (2016). Fault mirrors in seismically active fault zones: A fossil of small earthquakes at shallow depths. *Geophysical Research Letters*, *43*, 1950–1959. https://doi.org/10.1002/2015GL066882

Lee, Y.-H., Hsieh, M.-L., Lu, S.-D., Shih, T.-S., Wu, W.-Y., Sugiyama, Y., et al. (2003). Slip vectors of the surface rupture of the 1999 Chi-Chi earthquake, western Taiwan. *Journal of Structural Geology*, *25*(11), 1917–1931. https://doi.org/10.1016/S0191-8141(03)00039-7

Lin, A., Fu, B., Guo, J., Zeng, Q., Dang, G., He, W., & Zhao, Y. (2002). Co-seismic strike-slip and rupture length produced by the 2001 M_s 8.1 Central Kunlun earthquake. *Science*, *296*(5575), 2015–2017. https://doi.org/10.1126/science.1070879

Litchfield, N. J., Villamor, P., Dissen, R. J., Nicol, A., Barnes, P. M., Barrell, D. J. A., et al. (2018). Surface rupture of multiple crustal faults in the 2016 M_w 7.8 Kaikōura, New Zealand, earthquake. *Bulletin of the Seismological Society of America*, *108*(3B), 1496–1520. https://doi.org/10.1785/0120170300

Mizoguchi, K., Uehara, S. I., & Ueta, K. (2012). Surface fault ruptures and slip distributions of the M_w 6.6 11 April 2011 Hamadoori, Fukushima Prefecture, Northeast Japan, earthquake. *Bulletin of the Seismological Society of America*, *102*(5), 1949–1956. https://doi.org/10.1785/0120110308

Otsubo, M., Miyashita, Y., Miyakawa, A., & Miyawaki, M. (2013). Slickenlines on fault scarps along Yunodake fault caused by an earthquake in Iwaki-city (Fukushima Prefecture, Japan) on April 11, 2011. *Journal of the Geological Society of Japan*, *119*(9), XIII–XIV. https://doi.org/10.5575/geosoc.2013.0022

Otsubo, M., Shigematsu, N., Imanishi, K., Ando, R., Takahashi, M., & Azuma, T. (2013). Temporal slip change based on curved slickenlines on fault scarps along Itozawa fault caused by 2011 Iwaki earthquake, northeast Japan. *Tectonophysics*, *608*, 970–979. https://doi.org/10.1016/j.tecto.2013.07.022

Otsuki, K., Minagawa, J., Aono, M., & Ohtake, M. (1997). On the curved striations of Nojima seismic fault engraved at the 1995 Hyogoken-Nambu earthquake, Japan. *Journal of the Seismological Society of Japan*, *49*, 451–460.

Palmer, A. C., & Rice, J. R. (1973). The growth of slip surfaces in the progressive failure of over-consolidated clay. *Proceedings of the Royal Society of London*, *332*, 527–548.
Pan, J., Li, H., Si, J., Pei, J., Fu, X., Chevalier, M. L., & Liu, D. (2014). Rupture process of the Wenchuan earthquake (M_w 7.9) from surface ruptures and fault stations characteristics. *Tectonophysics*, *619*, 13–28.
Perrin, C., Manighetti, I., Ampuero, J.-P., Cappa, F., & Gaudemer, Y. (2016). Location of largest earthquake slip and fast rupture controlled by along-strike change in fault structural maturity due to fault growth. *Journal of Geophysical Research: Solid Earth*, *121*, 3666–3685. https://doi.org/10.1002/2015JB012671
Petit, J. P. (1987). Criteria for the sense of movement on fault surfaces in brittle rocks. *Journal of Structural Geology*, *9*(5–6), 597–608. https://doi.org/10.1016/0191-8141(87)90145-3
Philip, H., & Megard, F. (1977). Structural analysis of the superficial deformation of the 1969 Pariahuanca earthquakes (Central Peru). *Tectonophysics*, *38*(3–4), 259–278. https://doi.org/10.1016/0040-1951(77)90214-1
Philip, H., & Meghraoui, M. (1983). Structural analysis and interpretation of the surface deformations of the El Asnam Earthquake of October 10, 1980. *Tectonics*, *2*(1), 17–49. https://doi.org/10.1029/TC002i001p00017
Philip, H., Rogozhin, E., Cisternas, A., Bousquet, J. C., Borisov, B., & Karakhanian, A. (1992). The Armenian earthquake of 1988 December 7: Faulting and folding, neotectonics and palaeoseismicity. *Geophysical Journal International*, *110*(1), 141–158. https://doi.org/10.1111/j.1365-246X.1992.tb00718.x
Power, W. L., & Tullis, T. E. (1989). The relationship between slickenside surfaces in fine-grained quartz and the seismic cycle. *Journal of Structural Geology*, *11*(7), 879–893. https://doi.org/10.1016/0191-8141(89)90105-3
Power, W. L., Tullis, T. E., Brown, S. R., Boitnott, G. N., & Scholz, C. H. (1987). Roughness of natural fault surfaces. *Geophysical Research Letters*, *14*(1), 29–32. https://doi.org/10.1029/GL014i001p00029
Pucci, S., De Martini, P. M., Civico, R., Villani, F., Nappi, R., Ricci, T., et al. (2017). Coseismic ruptures of the 24 August 2016, M_w 6.0 Amatrice earthquake (Central Italy). *Geophysical Research Letters*, *44*, 2138–2147. https://doi.org/10.1002/2016GL071859
Renard, F., Candela, T., & Bouchaud, E. (2013). Constant dimensionality of fault roughness from the scale of micro-fractures to the scale of continents. *Geophysical Research Letters*, *40*, 83–87. https://doi.org/10.1029/2012GL054143
Ripperger, J., Ampuero, J. P., Mai, P. M., & Giardini, D. (2007). Earthquake source characteristics from dynamic rupture with constrained stochastic fault stress. *Journal of Geophysical Research*, *112*, B04311. https://doi.org/10.1029/2006JB004515
Shimamoto, T. (1996). Surface faults and damage associated with the 1995 Neftegorsk earthquake. *Journal of the Geological Society of Japan*, *102*(10), 894–907. https://doi.org/10.5575/geosoc.102.894
Sieh, K. E. (1978a). Slip along the San Andreas fault associated with the great 1857 earthquake. *Bulletin of the Seismological Society of America*, *68*, 1421–1448.
Sieh, K. E. (1978b). Central California foreshocks of the great 1857 earthquake. *Bulletin of the Seismological Society of America*, *68*, 1731–1749.
Slemmons, D. B. (1957). Geological effects of the Dixie Valley-Fairview Peak, Nevada, earthquakes of December 16, 1954. *Bulletin of the Seismological Society of America*, *47*, 353–375.
Somerville, P. G., Smith, N. F., Graves, R. W., & Abrahamson, N. A. (1997). Modification of empirical strong ground motion attenuation relations to include the amplitude and duration effects of rupture directivity. *Seismological Research Letters*, *68*(1), 199–222. https://doi.org/10.1785/gssrl.68.1.199
Spudich, P., Guatteri, M., Otsuki, K., & Minagawa, J. (1998). Use of fault striations and dislocation models to infer tectonic shear stress during the 1995 Hyogo-ken Nanbu (Kobe) earthquake. *Bulletin of the Seismological Society of America*, *88*, 413–427.
Tanaka, M., Asano, K., Iwata, T., & Kubo, H. (2014). Source rupture process of the 2011 Fukushima-ken Hamadori earthquake: How did the two subparallel faults rupture? *Earth, Planets and Space*, *66*, 101. https://doi.org/10.1186/1880-5981-66-101
Toda, S., & Tsutsumi, H. (2013). Simultaneous reactivation of two, subparallel, inland normal faults during the M_w 6.6 11 April 2011 Iwaki earthquake triggered by the M_w 9.0 Tohoku-oki, Japan, earthquake. *Bulletin of the Seismological Society of America*, *103*(2B), 1584–1602. https://doi.org/10.1785/0120120281
Toy, V. G., Niemeijer, A., Renard, F., Morales, L., & Wirth, R. (2017). Striation and slickenline development on quartz fault surfaces at crustal conditions: Origin and effect on friction. *Journal of Geophysical Research: Solid Earth*, *122*, 3497–3512. https://doi.org/10.1002/2016JB013498
Treiman, J. A., Kendrick, K. J., Bryant, W. A., Rockwell, T. K., & McGill, S. F. (2002). Primary surface rupture associated with the M_w 7.1 16 October 1999 Hector Mine earthquake, San Bernardino County, California. *Bulletin of the Seismological Society of America*, *92*(4), 1171–1191. https://doi.org/10.1785/0120000923
Twiss, R. J., Protzman, G. M., & Hurst, S. D. (1991). Theory of slickenline patterns based on the velocity gradient tensor and microrotation. *Tectonophysics*, *186*(3-4), 215–239. https://doi.org/10.1016/0040-1951(91)90360-5
Ulrich, T., Gabriel, A. A., Ampuero, J. P., & Xu, W. (2019). Dynamic viability of the 2016 M_w 7.8 Kaikōura earthquake cascade on weak crustal faults. *Nature Communications*, *10*, 1213. https://doi.org/10.1038/s41467-019-09125-w
Villani, F., Pucci, S., Civico, R., De Martini, P. M., Cinti, F. R., & Pantosti, D. (2018). Surface faulting of the 30 October 2016 M_w 6.5 Central Italy earthquake: Detailed analysis of a complex coseismic rupture. *Tectonics*, *37*, 3378–3410. https://doi.org/10.1029/2018TC005175
Wei, S., Fielding, E., Leprince, S., Sladen, A., Avouac, J. P., Helmberger, D., et al. (2011). Superficial simplicity of the 2010 El Mayor-Cucapah earthquake of Baja California in Mexico. *Nature Geoscience*, *4*(9), 615–618. https://doi.org/10.1038/ngeo1213
Witkind, I. (1962). Geologic features of the earthquake at Hebgen Lake, Montana, August 17, 1959. *Bulletin of the Seismological Society of America*, *52*(2), 163–180. https://pubs.geoscienceworld.org/bssa/article-lookup/52/2/163
Xu, S., Nieto-Samaniego, A. F., & Alaniz-Álvarez, S. A. (2013). Origin of superimposed and curved slickenlines in San Miguelito range, Central México. *Geologica Acta*, *11*, 103–112. https://doi.org/10.1344/105.000001760
Xu, X., Wen, X., Yu, G., Chen, G., Klinger, Y., Hubbard, J., & Shaw, J. (2009). Coseismic reverse- and oblique-slip surface faulting generated by the 2008 M_w 7.9 Wenchuan earthquake, China. *Geology*, *37*(6), 515–518. https://doi.org/10.1130/G25462A.1
Yoshida, S., Koketsu, K., Shibazaki, B., Sagiya, T., Kato, T., & Yoshida, Y. (1996). Joint inversion of near- and far-field waveforms and geodetic data for the rupture process of the 1995 Kobe earthquake. *Journal of Physics of the Earth*, *44*(5), 437–454. https://doi.org/10.4294/jpe1952.44.437

JGR: Solid Earth

Supporting information for

On-fault geological fingerprint of earthquake rupture direction.

J. Kearse, Y. Kaneko

Contents of this file

Parameters	Value in the representative model	Values considered
Effective normal stress **σ**	7.4 (MPa/km down-dip distance)	5.0 – 10.0 (MPa/km down-dip distance)
Prestress (initial shear) along strike τ_{os}	cos(rake °) *0.55*σ	cos(rake °) *0.55*σ
Prestress (initial shear) along dip τ_{od}	sin(rake °) *0.55*σ	sin(rake °) *0.55*σ
Static friction μ_s	0.80	0.6 – 0.85
Dynamic friction μ_d	0.40	0.1 – 0.5
Characteristic slip distance D_c	0.30 m	0.2 – 3.0 m
Frictional cohesion in the top 5 km **C**	2.0 MPa	0.0 – 2.0 MPa
Seismic ratio, **S**	1.5	0.5 – 2.5
Dynamic stress drop at 7.5 km down-dip distance	7.2 MPa	3.0 – 25.0 MPa

Table S1. Stress and friction parameters for the representative cases shown in Figure 2, and ranges of different values considered.

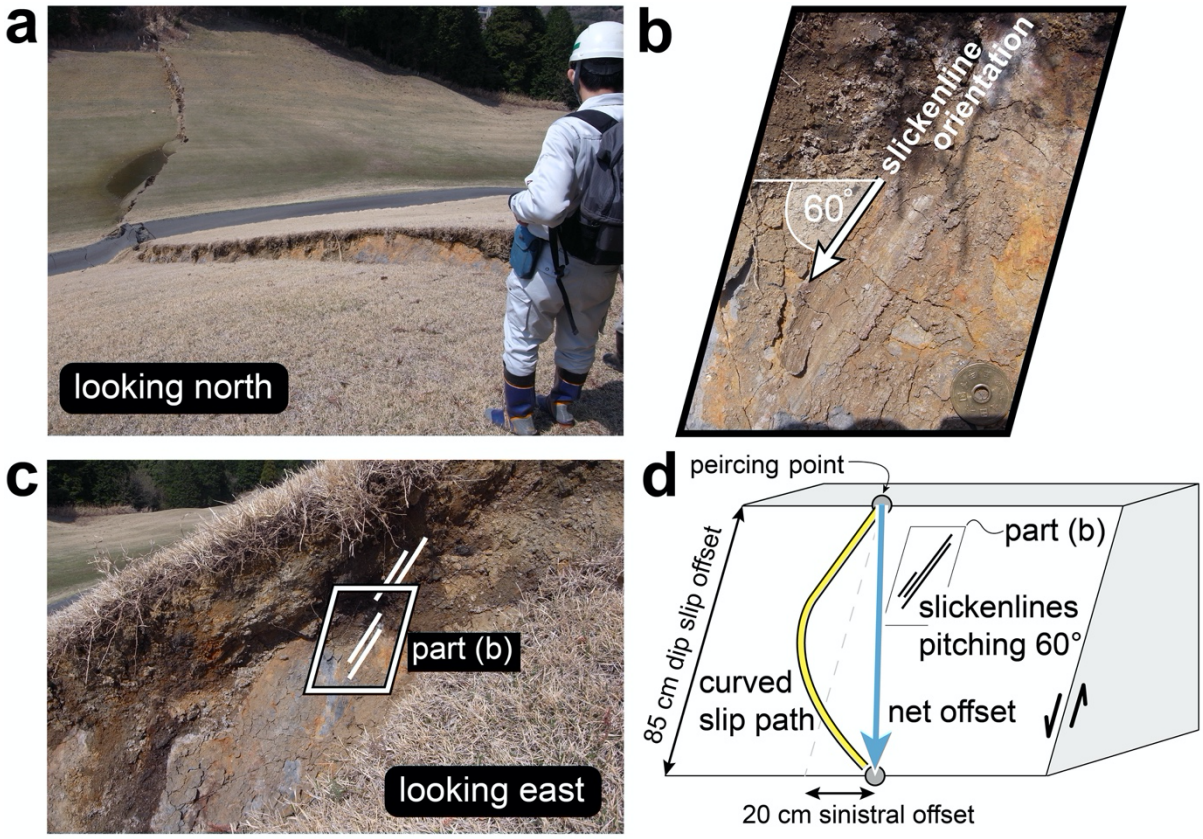

Figure S1. Surface rupture of the Yunodake fault (photographs and structural measurements provided by Kazuo Mizoguchi) (a) photograph showing the surface rupture trace at this site looking towards north (b) close-up of linear slickenlines observed on the fault plane and subsurface soils. Slickenlines pitch 60° north indicating a dextral component of motion (c) wider view of the slickenline observations in part b. (d) schematic block diagram showing the relationship between observed linear slickenlines (black), net offset defined by piercing points (blue), and the curved slip path (yellow).